Mon. Not. R. Astron. Soc. **000**, 000–000 (0000) Printed 7 December 2011 (MN LaTeX style file v2.2)

arXiv:1112.1402v1 [astro-ph.CO] 6 Dec 2011

A high resolution study of intergalactic O vi absorbers at $z \sim 2.3$

S. Muzahid[1]⋆, R. Srianand[1], J. Bergeron[2] and P. Petitjean[2]
[1] *Inter-University Centre for Astronomy and Astrophysics, Post Bag 4, Ganeshkhind, Pune 411 007, India*
[2] *Université Paris 6, UMR 7095, Institut d'Astrophysique de Paris-CNRS, 98bis Boulevard Arago, 75014 Paris, France*

Accepted. Received; in original form

ABSTRACT

We present a detailed study of the largest sample of intervening O vi systems in the redshift range $1.9 \leq z \leq 3.1$ detected in high resolution ($R \sim 45{,}000$) spectra of 18 bright QSOs observed with VLT/UVES. Based on Voigt profile and apparent optical depth analysis we find that (i) the Doppler parameters of the O vi absorption are usually broader than those of C iv (ii) the column density distribution of O vi is steeper than that of C iv (iii) line spread (δv) of the O vi and C iv are strongly correlated (at 5.3σ level) with δv(O vi) being systematically larger than δv(C iv) and (iv) δv(O vi) and δv(C iv) are also correlated (at $> 5\sigma$ level) with their respective column densities and with N(H i) (3 and 4.5σ respectively). The median column densities of H i, O vi, and C iv are found to be higher when low ions are present. N(C iv) and N(H i) are strongly correlated (at 4.3σ level). However, no significant correlation is found between N(O vi) and N(H i). These findings favor the idea that C iv and O vi absorption originate from different phases of a correlated structure and systems with large velocity spread are probably associated with overdense regions. The velocity offset between optical depth weighted redshifts of C iv and O vi absorption is found to be in the range $0 \leq |\Delta v(\text{O vi} - \text{C iv})| \leq 48$ km s^{-1} with a median value of 8 km s^{-1}.

We do not find any evidence for the ratios N(O vi)/N(H i), N(O vi)/N(C iv) and N(C iv)/N(H i) to evolve with z over the redshift range considered here. But a lack of systems with high N(O vi)/N(H i) ratio (i.e., ≥ -0.5 dex) for $z > 2.5$ is noticeable. Similar trend is also seen for the N(C iv)/N(H i) ratio. We compare the properties of O vi systems in our sample with that of low redshift ($z < 0.5$) samples from the literature and find that (i) the O vi components at low-z are systematically wider than at high-z with an enhanced non-thermal contribution to their b-parameter, (ii) the slope of the column density distribution functions for high and low-z are consistent, (iii) the range in gas temperature estimated from a subsample of well aligned absorbers is similar at both high and low-z, and (iv) $\Omega_{\text{O vi}} = (1.0 \pm 0.2) \times 10^{-7}$ for $N(\text{O vi}) > 10^{13.7}$ cm^{-2}, estimated in our high-z sample, is very similar to low-z estimations.

Key words: galaxies: quasar: absorption line – quasar – galaxies: intergalactic medium

1 INTRODUCTION

The study of low density intergalactic medium (IGM) is extremely important because it forms the primary reservoir of baryons throughout the cosmic ages. These baryons get accumulated into galaxies in the process of structure formation. The heavy elements produced in galaxies got transported to the IGM by means of outflows driven by supernovae or tidal interactions. Thus the IGM enrichment history provides useful constraints on the star formation history and contribution of various feedback mechanisms at different epochs. The tenuous IGM is detectable in the form of Lyα and heavy element absorption lines in the QSO spectra. Hence the observation of Lyα and metal lines are crucial to understand the interaction between galaxies and the surrounding IGM.

The observations of C iv and O vi absorption in QSO spectra have established the presence of heavy elements in the IGM unequivocally (Cowie et al. 1995a,b; Songaila & Cowie 1996; Bergeron et al. 2002; Simcoe et al. 2002; Carswell et al. 2002). The early observations of heavy elements in the high redshift universe were focused on C iv absorption, since it has strongest lines falling in the region free from Lyα contamination. Several high redshift surveys have ascertained that the cosmic density of C iv absorbers has not evolved substantially from redshift $z = 5$ to $z = 1.5$ (see Songaila 2001, 2005; Boksenberg et al. 2003; Pettini et al. 2003; Schaye et al. 2003). Due to lack of sufficient QSO sight lines, a clear picture is yet to emerge regarding the evolution of C iv at $z > 6$. However the limited sample of C iv absorbers available

---

⋆ E-mail: sowgat@iucaa.ernet.in

until now indeed indicates that a good fraction of metals may already be present in the IGM even at these high redshifts (Songaila 2006; Simcoe 2006; Ryan-Weber et al. 2006; Becker et al. 2006, 2009). The enrichment level found by these studies is consistent with [C/H] ~ -2.8.

Given the low metallicity, the direct detection of metals in the underdense regions [with overdensity, $\delta(\equiv n_{\rm H}/\overline{n}_{\rm H}) \ll 10$], which occupy most of the volume of the universe at any given epoch, is beyond the reach of the present day large telescopes. Statistical methods like pixel analysis are used instead (Ellison et al. 2000; Schaye et al. 2003; Aracil et al. 2004; Aguirre et al. 2005, 2008; Scannapieco et al. 2006; Pieri et al. 2006). They show that metals must be present even in the underdense regions. However the fractional volume occupied by the metals is still unknown.

Even in regions where metal absorption is detected directly, it is unclear what are the main physical processes that maintain the ionization state of the gas. In general, it is believed that photoionization by the meta-galactic UV background keeps the gas ionized. On the other hand, the winds that seed the IGM with metals and the accretion shocks in the evolving density fields may also provide sufficient mechanical feedback to collisionally ionize the gas. Therefore, it is crucial to simultaneously study different species covering a wide range of ionization states to get a better understanding of the metal enrichment and the different ionizing mechanisms at play.

Under photoionization by UV background, the O vi absorption is generally produced from regions of low-density having high ionization parameter. In addition, the high cosmic abundance of oxygen makes O vi a good tracer of metal-enrichment in the low-density IGM. In fact photoionization seems to be a viable process for most of the high redshift O vi absorbers (Bergeron et al. 2002; Carswell et al. 2002; Bergeron & Herbert-Fort 2005). On the other hand, hydrodynamical simulations (Cen & Ostriker 1999; Davé et al. 1999, 2001; Fang & Bryan 2001; Kang et al. 2005; Smith et al. 2011; Cen & Chisari 2011) suggest that a considerable amount of baryons could reside in the warm-hot phase of the intergalactic medium (called WHIM with $T \approx 10^5-10^7$ K) and this fraction evolves with redshift. Highly ionized species of oxygen such as O vi, O vii and O viii can be useful probes of the WHIM. In the optical regime, O vi is the best species to probe relatively cooler phase (i.e., $T \sim 3\times10^5$ K) of the WHIM because, the ionization fraction of O vi has its maximum around this temperature in case of collisional ionization. Indeed, it has been suggested that a large fraction of the O vi absorption associated with the IGM (Simcoe et al. 2002, 2006) and high-z damped Lyα systems (Fox et al. 2007) may originate from collisionally ionized gas. Thus the origin of the ionization of the intergalactic O vi absorbers is a matter of debate.

Numerous extragalactic O vi systems have been detected at $z < 0.5$ with the *Far Ultraviolet Spectroscopic Explorer* (*FUSE*) and *Hubble Space Telescope* (*HST*) (e.g., Tripp et al. 2000; Stocke et al. 2006; Danforth et al. 2006; Tripp et al. 2008; Thom & Chen 2008; Wakker & Savage 2009; Lehner et al. 2009; Tumlinson et al. 2011). However these studies could not establish convincingly whether O vi absorbers are predominantly tracing the WHIM gas or not. They seem to arise in either high metallicity photoionized (e.g., Oppenheimer & Davé 2009) or low metallicity collisionally ionized (e.g., Smith et al. 2011) gas loosely associated with galaxies. An alternative tool to detect the WHIM, which is independent of the metal enrichment, is to search for thermally-broadened Lyα absorbers (BLAs) (Sembach et al. 2004; Richter et al. 2004, 2006; Danforth et al. 2010; Savage et al. 2010, 2011). However, until now the WHIM detection through BLAs has also been ambiguous. The few detections of Ne viii in the FUV regime (Savage et al. 2005; Narayanan et al. 2009, 2011) and O vii in the soft X-ray regime (e.g., Nicastro et al. 2005a,b; Buote et al. 2009; Fang et al. 2010; Zappacosta et al. 2010) possibly hint the existence of the WHIM.

At high redshift ($z > 2$) previous studies (Simcoe et al. 2002, 2004; Carswell et al. 2002; Bergeron et al. 2002; Bergeron & Herbert-Fort 2005; Schaye et al. 2007; Frank et al. 2010a,b) have already provided important insights into the properties of O vi absorbers. Here we present a detailed analysis of O vi absorbers using a sample which is twice as large as the previous sample of high-z intervening O vi systems studied at high resolution.

This paper is organized as follows. In section 2 we describe the observations and the data reduction procedure for our data sample. In section 3 we describe the line identification strategy and present the O vi and C iv sample and various physically motivated subsamples. In section 4 we analyze the distributions of O vi Voigt profile parameters and compared them with those of C iv. In this section we also compare the properties of O vi absorption at high and low redshift. In section 5 we discuss the line kinematics of O vi and C iv absorption. In section 6 we present analysis based on total column densities with results of photoionization model as guidelines. In section 7 we summarize our results.

Throughout this paper we use the following cosmological parameters for a flat universe : $\Omega_{\rm m} = 0.3$, $\Omega_\Lambda = 0.7$, $\Omega_b h^2 = 0.02$ and $H_0 = 71$ km s^{-1}Mpc^{-1}. The solar relative abundances are taken to be default values used in CLOUDY v(07.02), i.e., log (C/H)$_\odot = -3.61$ and log (O/H)$_\odot = -3.31$.

2 OBSERVATIONS

The spectra used in this study were obtained with the Ultra-Violet and Visible Echelle Spectrograph (UVES) (Dekker et al. 2000) mounted on the ESO Kueyen 8.2 m telescope at the Paranal observatory in the course of the ESO-VLT large programme "The Cosmic Evolution of the IGM" (Bergeron et al. 2004). This large programme provided a homogeneous set of 18 QSO sight lines with QSO emission redshifts ranging from 2.1 to 3.3. The raw data were reduced using the UVES pipeline (Ballester et al. 2000) which is available as a dedicated context of the MIDAS data reduction software. The main function of the pipeline is to perform a precise inter-order background subtraction for science frames and master flat fields, and to apply an optimal extraction to retrieve the object signal, rejecting cosmic ray impacts and performing sky subtraction at the same time. The reduction is checked step-by-step. Wavelengths are corrected to vacuum-heliocentric values using standard conversion equations (Edlén 1966; Stumpff 1980). Combination of individual exposures is performed by adjusting the flux in each individual exposures to the same level and inverse variance weighting the flux in each pixel. Great care was taken in computing the error spectrum while combining the individual exposures. Our final error in each pixel is the quadratic sum of the weighted mean of errors in the different spectra and the scatter in the individual flux measurements. Errors in individual pixels obtained by this method are consistent with the rms dispersion around the best fitted continuum in regions free of absorption lines. The final combined spectrum covers the wavelength range of 3000 to 10,000 Å with occasional narrow gaps in the red. During the observations, the 2×2 binning mode was used yielding a binned pixel size of 2.0 – 2.4 km s^{-1}. A typical signal-to-noise ratio (S/N) $\sim$ 30 – 40 and 60 – 70 per

Table 1. Details of O VI systems

QSO	$z_{\rm em}$	$z_{\rm min}$	$z_{\rm max}$	$z_{\rm sys}$	log N(H I)	log N(O VI)	log N(C IV)	Class[1]	Case[2]	$\delta_{\rm type}$ [3]	δv(O VI) (km s^{-1})	δv(C IV) (km s^{-1})	$\lvert\Delta v$(O VI – C IV)$\rvert$ (km s^{-1})	Low Ions[6]
HE 1341–1020	2.135	1.983	2.083	1.9982	13.77±0.04	13.71±0.04	12.22±0.05	*dd*	A	0	24.3	19.7	4.6	No
				2.0414	15.70±0.07	14.01±0.12	13.25±0.09	*bd*	B	+1	88.6	36.9	...	Yes
				2.0850	15.10±0.02	13.79±0.08	12.98±0.06	*bb*	B	−1	23.6	91.8	...	No
Q 0122–380	2.190	1.989	2.137	2.0349	15.54±0.06	13.70±0.09	13.10±0.04	*dd*	B	−1	59.8	77.7	...	No
				2.0626	12.49±0.04	13.47±0.05	12.94±0.01	*bd*	A	0	45.1	19.3	2.0	No
PKS 1448–232	2.220	2.008	2.166	2.1099	13.86±0.02	14.48±0.07	13.16±0.03	*dd*	A	0	56.0	35.4	3.3	No
				2.1660	15.52±0.36	14.29±0.13	13.48±0.18	*dd*	A/B	0	272.8	166.4	13.4	Yes
PKS 0237–23	2.222	1.954	2.168	1.9878[4]	13.64±0.01	13.41±0.06	≤ 11.97	*dd*	A	0	41.3	0.0	...	No
				2.0108[4]	14.51±0.06	13.15±0.05	≤ 11.93	*dd*	A	0	26.5	0.0	...	No
				2.0412	16.24±0.04	13.16±0.07	12.61±0.06	*bd*	B	−1	31.0	36.8	...	No
				2.0422	≤ 13.48	14.30±0.07	13.66±0.05	*bd*	A	0	47.7	40.7	7.2	No
HE 0001–2340	2.263	1.982	2.209	2.0323	16.07±0.16	13.89±0.06	12.85±0.13	*bd*	B	0	50.3	64.2	15.3	No
				2.1617	15.61±0.22	13.82±0.06	12.76±0.06	*dd*	B	0	80.4	80.7	19.2	No
Q 0109–3518	2.404	1.980	2.347	2.0226	14.99±0.05	14.24±0.14	12.52±0.03	*bd*	B	+1	60.1	41.0	...	Yes
				2.1415	15.01±0.53	13.52±0.06	11.70±0.08	*dd*	B	0	60.1	16.6	5.3	No
HE 2217–2818	2.414	1.959	2.357	2.0160	15.03±0.02	13.77±0.13	12.80±0.05	*bb*	B	0	86.8	86.0	0.1	No
				2.0748	14.12±0.01	14.32±0.01	12.85±0.01	*dd*	A/B	−1	37.8	92.0	...	No
				2.1808	16.06±0.04	14.19±0.23	13.53±0.07	*dd*	A/B	0	178.2	115.1	46.4	Yes
Q 0329–385	2.435	2.018	2.378	2.0764	13.70±0.08	13.26±0.05	13.21±0.01	*bd*	A	0	21.3	19.2	4.2	No
				2.1470[4]	14.73±0.21	13.95±0.18	≤ 12.89	*dd*	A	0	120.1	0.0	...	No
				2.2489[4]	13.51±0.30	14.25±0.49	≤ 12.82	*dd*	A	0	107.4	0.0	...	No
				2.2510	15.82±0.55	14.86±0.16	14.41±0.08	*dd*	B	0	127.4	84.4	10.4	Yes
				2.3139	14.23±0.10	13.30±0.10	12.35±0.12	*dd*	B	0	48.2	43.1	12.9	No
				2.3520	13.05±0.01	14.09±0.09	13.50±0.08	*dd*	A	0	41.2	27.3	1.0	Yes
				2.3639	14.85±0.09	13.73±0.03	12.40±0.10	*dd*	A	0	64.8	57.8	1.2	No
				2.3738	15.26±0.01	14.26±0.08	12.66±0.06	*dd*	A	0	153.0	96.6	0.8	No
HE 1158–1843	2.449	1.980	2.391	2.2354	14.74±0.02	13.71±0.17	12.99±0.12	*dd*	A	0	47.1	35.4	2.1	No
				2.2660	15.88±0.05	13.68±0.05	13.68±0.04	*bd*	A/B	+1	142.4	29.7	...	Yes
HE 1347–2457	2.611	1.985	2.551	2.1162	15.16±0.07	14.57±0.07	13.43±0.07	*bd*	A/B	+1	91.2	63.2	...	Yes
				2.2349	15.06±0.02	14.43±0.47	13.24±0.11	*dd*	A	0	195.9	187.3	10.6	No
				2.3289	16.45±0.04	14.63±0.04	14.26±0.04	*bb*	B	−1	59.1	99.5	...	Yes
				2.3327[4]	13.89±0.02	13.26±0.03	≤ 12.02	*dd*	A	0	45.9	0.0	...	No
				2.3422[4]	14.82±0.30	13.45±0.09	≤ 12.30	*dd*	A	0	56.7	0.0	...	No
				2.3700	14.96±0.10	14.08±0.05	12.95±0.08	*bd*	A	0	77.8	62.7	16.9	Yes
				2.4455	15.14±0.47	13.69±0.26	12.62±0.17	*bd*	B	0	67.7	64.7	0.8	No
Q 0453–423	2.658	2.001	2.597	2.1694	13.75±0.03	14.27±0.05	12.65±0.05	*bb*	A	+1	119.2	80.5	...	No
				2.2765	16.29±0.06	14.87±0.32	14.78±0.23	*bb*	B	−1	179.6	149.8	...	Yes
				2.3978	15.14±0.09	14.97±0.36	14.47±0.18	*bb*	A	0	186.0	156.2	48.5	Yes
				2.4435	15.37±0.05	14.44±0.24	13.76±0.35	*bb*	A/B	0	181.4	142.8	6.9	Yes
				2.5028	15.77±0.02	13.99±0.03	13.71±0.34	*bb*	B	−1	74.7	78.3	...	Yes
				2.5214	15.31±0.04	13.58±0.19	12.58±0.15	*bb*	B	−1	51.6	32.5	...	No
				2.5371[4]	14.67±0.08	13.42±0.07	≤ 12.29	*dd*	A	0	45.2	0.0	...	No
PKS 0329–255	2.703	2.080	2.641	2.2044	15.44±0.22	14.61±0.24	13.32±0.21	*bd*	B	+1	176.9	144.7	...	No
				2.3284	16.20±0.12	13.96±0.30	13.49±0.70	*bb*	B	−1	93.9	186.8	...	Yes
				2.3896[4]	14.22±0.12	13.37±0.02	≤ 12.00	*bb*	A	+1	0.0	0.0	...	No
				2.4253	15.58±0.05	13.86±0.12	13.25±0.19	*dd*	B	0	65.8	50.0	9.7	Yes
				2.5687	14.78±0.04	13.58±0.44	12.52±0.26	*dd*	A	0	42.8	48.0	6.8	No
Q 0002–422	2.767	2.064	2.704	2.1767[4]	13.62±0.01	13.72±0.04	≤ 12.02	*bd*	A	0	52.6	0.0	...	No
				2.2200[4]	14.95±0.02	13.80±0.32	≤ 12.09	*dd*	A/B	0	51.8	0.0	...	No
				2.2621	15.47±0.04	13.67±0.11	12.43±0.03	*bd*	B	0	44.5	38.5	12.0	No
				2.5395	14.55±0.03	13.79±0.01	12.48±0.02	*dd*	A	0	61.5	29.1	7.2	No
				2.6075	14.72±0.03	14.10±0.05	12.14±0.05	*bd*	A	0	70.4	34.9	7.7	No
HE 0151–4326	2.789	2.043	2.726	2.0885	15.16±0.06	13.75±0.10	12.81±0.29	*dd*	B	0	35.3	33.8	2.7	No
				2.1699	15.25±0.02	13.86±0.07	13.04±0.01	*bd*	B	0	43.5	27.5	9.7	No
				2.2010	15.39±0.03	14.23±0.13	13.12±0.19	*bd*	B	0	131.6	146.9	1.1	Yes
				2.3598[4]	14.03±0.03	13.45±0.10	≤ 12.24	*bd*	A	0	47.6	0.0	...	No
				2.4681	13.25±0.22	14.38±0.54	13.43±0.06	*dd*	A	0	73.3	65.9	15.0	Yes
				2.4927	14.77±0.01	14.16±0.27	13.51±0.03	*bd*	A	0	120.6	42.6	18.1	No
				2.5053	15.01±0.02	14.19±0.08	12.47±0.16	*bb*	A	−1	118.1	117.5	...	No
				2.5235	14.81±0.56	13.94±0.23	12.30±0.15	*bb*	A	−1	0.0	0.0	...	No
HE 2347–4342	2.871	2.301	2.806	2.3475	16.17±0.11	13.74±0.11	13.49±0.01	*bd*	B	0	34.7	25.6	9.7	Yes
				2.4382	14.84±0.02	14.38±0.11	12.98±0.15	*bd*	B	0	126.8	74.7	11.0	No
				2.6346	14.84±0.38	14.31±0.28	13.08±0.14	*bb*	A	0	126.0	64.4	26.5	No
				2.6498	15.12±0.06	14.07±0.08	12.66±0.06	*bd*	A/B	0	114.8	79.8	2.1	No
				2.7121	14.85±0.07	13.96±0.06	12.27±0.11	*bd*	B	−1	86.8	46.2	...	No
				2.7356	16.50±0.28	14.41±0.11	14.08±0.10[5]	*bb*	B	−1	58.2	0.0	...	Yes
				2.7456	14.42±0.04	13.47±0.04	.....[7]	*bd*	A	0	71.0	0.0	...	No
HE 0940–1050	3.084	2.458	3.016	2.5167	15.37±0.03	13.89±0.01	12.84±0.07	*bb*	B	0	62.2	74.8	16.6	No
				2.6433	15.56±0.15	13.94±0.07	13.16±0.07	*bb*	B	−1	90.9	89.5	...	No
				2.6580	15.41±0.02	13.79±0.01	13.40±0.05	*dd*	B	0	68.5	32.8	5.1	Yes
				2.8265	16.72±0.37	14.50±0.06	14.17±0.16	*bb*	B	−1	136.6	377.0	...	Yes
				2.8345	16.66±0.06	14.40±0.01	14.27±0.24	*bb*	B	−1	83.2	91.4	...	Yes
				2.9377	14.77±0.03	13.86±0.12	12.94±0.05	*bb*	A	−1	101.3	70.2	...	Yes
				2.9401	14.67±0.01	14.16±0.06	12.64±0.09	*bb*	A/B	+1	92.2	71.9	...	Yes
Q 0420–388	3.117	2.625	3.048	2.6615	15.44±0.03	14.58±0.03	14.37±0.18	*bb*	B	−1	229.2	89.6	...	Yes
				2.8100	15.29±0.03	13.48±0.05	12.53±0.04	*bd*	B	0	46.3	17.3	5.1	No
PKS 2126–158	3.280	2.508	3.209	2.9073	16.16±0.04	13.92±0.17	13.63±0.23	*bd*	B	0	68.7	82.5	7.6	Yes

Table Notes – Underlined lines of sight are common to Bergeron & Herbert-Fort (2005). [1] Class is based on the O VI profiles. The systems with both the doublets are unblended (partially blended) are marked by "*dd*" ("*bb*"). In "*bd*" systems one of the doublets is blended. [2] Case is based on the presence of unsaturated Lyman-series line. "Case A" systems have at least one of the available Lyman-series line unsaturated. In "Case B", systems all the available Lyman-series are saturated. "Case A/B" are the cases where some parts of H I absorption are unsaturated. [3] $\delta_{\rm type}$ is based on the robust measurement of O VI line spread. $\delta_{\rm type}$ of +1 and −1 indicate upper and lower limits on line spread whereas $\delta_{\rm type}$ of 0 represents robust measurement. [4] "O VI only" system. [5] C IV column density is taken from Agafonova et al. (2007). [6] Indicating the presence of low ions. [7] C IV falls in the spectral gap.

Table 2. Systems with upper limits on N(O vi)

QSO	$z_{\rm sys}$	log (column density) N(H i)	log (column density) N(C iv)	log (column density) $\leq N$(O vi)	δv(C iv) (km s^{-1})	Low Ions
PKS 1448–232	1.9516	14.94 ± 0.05	12.89 ± 0.01	13.90^a	23.9	No
PKS 1448–232	1.9781	15.07 ± 0.07	12.64 ± 0.03	13.77^a	35.6	No
HE 0001–2340	2.1634	14.71 ± 0.04	11.92 ± 0.06	12.81^a	20.2	No
Q 0109–3518	2.0463	16.09 ± 0.41	14.07 ± 0.10	14.38	172.3	Yes
HE 2217–2818	2.0374	15.46 ± 0.07	12.16 ± 0.06	12.91^a	23.3	No
HE 2217–2818	2.1553	14.13 ± 0.02	12.48 ± 0.02	12.94	23.9	No
HE 1158–1843	2.0348	15.43 ± 0.29	12.61 ± 0.03	13.28^a	38.8	No
HE 1158–1843	2.0407	15.52 ± 0.07	12.51 ± 0.03	13.17^a	29.1	No
HE 1347–2457	1.9750	14.76 ± 0.02	12.64 ± 0.04	13.60^a	45.7	No
Q 0453–423	2.4163	15.00 ± 0.01	12.56 ± 0.02	13.81	28.5	No
PKS 0329–255	2.1611	15.95 ± 0.09	12.41 ± 0.05	13.23	29.4	Yes
PKS 0329–255	2.2953	14.82 ± 0.03	11.96 ± 0.09	12.57^a	19.1	No
PKS 0329–255	2.4208	14.86 ± 0.02	12.53 ± 0.16	14.31	41.7	Yes
PKS 0329–255	2.5868	15.14 ± 0.02	12.29 ± 0.04	12.76^a	15.9	Yes
Q 0002–422	2.3647	12.28 ± 0.02	12.14 ± 0.03	12.56^a	15.3	No
HE 0151–4326	2.4013	15.13 ± 0.01	12.56 ± 0.08	13.97	60.5	Yes
HE 0151–4326	2.4158	13.35 ± 0.01	13.03 ± 0.01	14.19	23.4	Yes
HE 0151–4326	2.4196	13.04 ± 0.02	12.75 ± 0.01	12.57^a	21.7	Yes
HE 0151–4326	2.5199	15.40 ± 0.02	12.28 ± 0.03	12.56^a	25.9	Yes
HE 2347–4342	2.3132	15.89 ± 0.71	13.73 ± 0.07	14.82	194.8	Yes
HE 2347–4342	2.3317	15.58 ± 0.06	12.38 ± 0.04	14.31	35.9	Yes
HE 0940–1050	2.3307	16.32 ± 0.43	14.85 ± 0.23	15.19	197.2	Yes
HE 0940–1050	2.4090	15.94 ± 0.14	13.56 ± 0.16	14.18	35.2	Yes
HE 0940–1050	2.6136	15.32 ± 0.02	12.56 ± 0.02	13.58	31.6	No
HE 0940–1050	2.6679	15.60 ± 0.06	13.78 ± 0.09	14.11	68.6	Yes
Q 0420–388	2.8235	15.52 ± 0.03	13.73 ± 0.10	14.17	132.4	Yes
Q 0420–388	2.8496	14.25 ± 0.04	12.70 ± 0.13	14.06	64.9	No
Q 0420–388	2.9519	15.35 ± 0.01	12.72 ± 0.10	13.93	58.2	Yes
PKS 2126–158	2.3889	13.92 ± 0.02	13.05 ± 0.01	13.66	19.7	No
PKS 2126–158	2.5537	14.05 ± 0.04	13.10 ± 0.05	14.55	28.2	No
PKS 2126–158	2.6790	14.00 ± 0.03	14.24 ± 0.03	14.24	33.9	Yes
PKS 2126–158	2.8194	15.61 ± 0.02	13.50 ± 0.08	14.60	170.5	No
PKS 2126–158	2.9634	15.85 ± 0.03	13.27 ± 0.09	14.08	91.3	Yes

Table Note – ^{a}Unabsorbed continuum is seen at least in one the O vi doublets.

Table 3. List of Lyman limit systems with O vi detections

QSO	$z_{\rm sys}$	log N(H i)	log N(O vi)	log N(C iv)
PKS 0329–255	2.1584	17.53	12.99	12.86
Q 0002–422	2.1683	18.46	13.64	14.38
	2.3023	17.75	15.21	15.47
	2.4633	18.49	14.63	14.79
PKS 2126–158	2.6377	19.23	14.85	....^{a}
	2.7692	18.62	14.80	14.71

Table Note – ^{a} C iv falls in the spectral gap

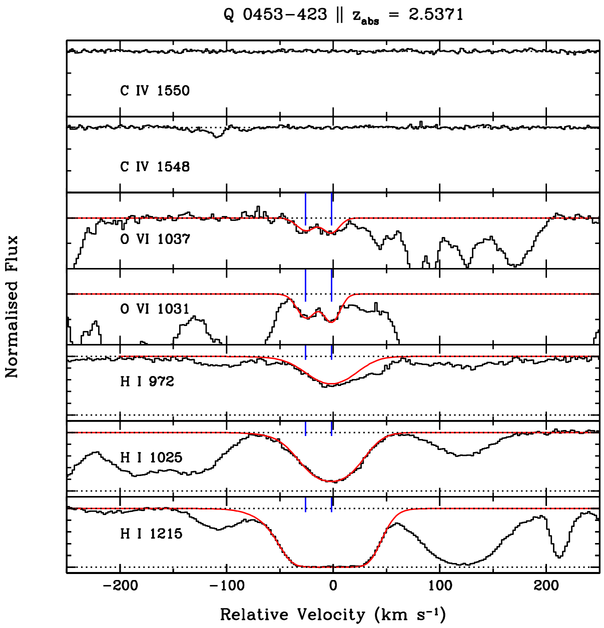

Figure 1. An example of O vi system without detectable associated C iv and other heavy elements absorption. The best fitted Voigt profiles of O vi and H i are over-plotted on the observed data. The vertical tick marks show the positions of the individual components. The absorption redshift that defines the zero velocity and the name of the background QSO are indicated at the top. We found 11 such systems in our sample.

pixel was achieved at 3300 and 5500 Å respectively. The typical final spectral resolution is $R \sim 45,000$ (FWHM ∼ 6.6 km s^{-1}) over the entire wavelength range. This spectral resolution allows us to resolve lines with b-parameter as narrow as ∼ 4 km s^{-1}. The unabsorbed QSO continuum is then fitted using low order polynomials extrapolated from wavelength ranges devoid of strong absorption lines. The detailed description of data calibration is presented in Aracil et al. (2004) and Chand et al. (2004).

3 DATA SAMPLE AND OBSERVABLES

In this section we describe our line identification strategy, absorption line measurement techniques and various physically motivated subsamples we use for statistical studies.

For the analysis presented here we concentrate on the intervening O vi and C iv systems defined as those with apparent ejection velocity larger than 5000 km s^{-1} relative to the QSO emission redshift (using $z_{\rm em}$ given in Rollinde et al. 2005; Scannapieco et al. 2006). The detailed discussions of the associated systems towards QSOs in our sample can be found in Fox et al. (2008).

Following Scannapieco et al. (2006) we define a system by grouping together all the components whose separation from their nearest neighbor is less than a linking length, $v_{\rm link}$ = 100 km s^{-1}. These authors have shown that the absorber's properties and in particular the velocity clustering do not change much for velocities smaller than this. Note that the same convention was also adopted by Songaila (2005).

We have searched for O vi following two different approaches. (1) First we identify metal line doublets (e.g. C iv and/or Si iv) redshifted beyond the wavelength of the QSO Lyα emission and we look for O vi doublets around this redshift (i.e. within ∼ 100 km s^{-1} to the C iv or Si iv redshift). The presence of O vi is confirmed after checking the consistency in the optical depths of the two O vi lines. There are 104 C iv systems (see also D'Odorico et al. 2010) along the lines of sight we study over the redshift range where O vi is detectable with S/N > 10. In addition, there is a system ($z_{\rm abs}$ = 2.7356 towards HE 2347−4342) that is identified by the presence of Si iv doublets where the corresponding C iv doublets fall in the narrow wavelength range not covered by our UVES spectrum. The presence of C iv in this system has been confirmed by Agafonova et al. (2007). The total C iv column density in this system is taken from their measurement. Out of these 105 C iv systems, 72 show detectable O vi absorption. Details of the systems are given in Table 1. For the other 33 C iv systems, only upper limits on O vi column density can be obtained. These systems are listed in Table 2. Whenever possible we use rms error in the unabsorbed continuum at the expected position of the O vi doublets to estimate 3σ limit on column density using the same number of components and b-values as seen in C iv. In rest of the cases where there is strong Lyα absorption we use the z and b-values of C iv and generated the minimum O vi profile that explains the observed spectrum. This allows us to get only a conservative upper limit on N(O vi).

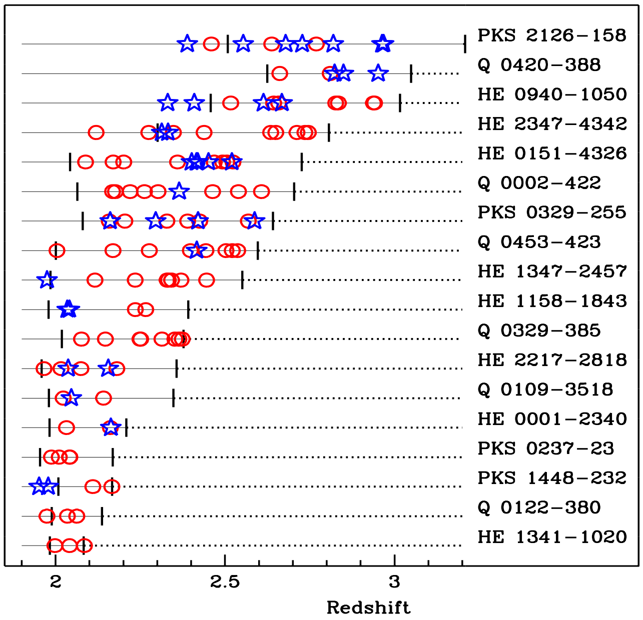

Figure 2. Schematic diagram showing the positions of the absorbers in redshift space along the lines of sight of the QSOs in our sample. The (red) circles indicate the redshifts of O VI systems whereas (blue) stars indicate the redshift of C IV systems where we have upper limits on N(O VI). The left and right vertical lines are the minimum and maximum redshifts along each line of sight. The horizontal dotted lines are just to guide the reader's eye.

(2) Secondly, we directly search for the O VI doublets in the Lyα forest. In fact, O VI absorption lines without detectable associated C IV and/or Si IV (and H I) can trace the highly ionized gas that originates from the WHIM with characteristic temperature $\sim 10^5$–10^7K predicted in some simulations (e.g., Cen & Ostriker 1999, 2006; Davé et al. 1999, 2001). For each of these identified coincidences we checked the consistency of the shape and optical depth ratios of the O VI doublets. We then checked for the presence of associated Lyα (and possibly higher Lyman series lines) at the redshift of the chosen O VI doublets. While the presence of associated Lyα absorption confirms the O VI identification, it need not be detectable in case O VI comes from collisionally ionized gas. Therefore, we do not impose the detection of Lyα absorption as a necessary criterion to confirm the O VI doublets. We found 12 systems from the presence of the O VI doublet only (an example is shown in Fig. 1). In all these cases associated H I is detected. For one of these systems ($z_{\rm abs} = 2.7456$ towards HE 2347–4342) the wavelength range corresponding to C IV absorption fall in a spectral gap, so that we could not probe the presence of C IV in this system. For the other 11 systems we do not detect any other metal. Apart for the $z_{\rm abs}$ = 2.1767 and 2.3598 systems towards Q 0002–422 and HE 0151–4326, respectively, all other systems show absorption from at least one of the higher Lyman series lines in addition to Lyα (i.e. at least Lyβ). Thus we are confident that these identifications of O VI are secure. However, as we look for the presence of both lines in the doublet it is possible that our method has missed some of the O VI only absorbers where absorption from one of the transitions (or both) is contaminated by Lyα absorption.

We have found six Lyman-limit systems (LLS) with detectable O VI listed in Table 3. There are 3 more LLS ($z_{\rm abs}$ = 2.7278 & 2.9676 towards PKS 2126–158 and $z_{\rm abs}$ = 2.4512 towards HE 0151–4326) where only upper limits on O VI column densities could be obtained. Note that all the LLS are excluded in the analysis presented in this paper. This is because N(H I) measurement in these systems are uncertain and they may not trace IGM gas which is of prime interest in this study.

The redshifts of all the intervening O VI absorbers (both detections and upper limits) are summarized in Fig. 2. For each line of sight (mentioned in the extreme right) the vertical tick mark on the left indicates the redshift above which the S/N per pixel of the corresponding spectrum is $>$ 10. This defines the minimum redshift ($z_{\rm min}$) for each line of sight as given in column #3 of Table 1 & 4. There are 7 systems listed in Table 4 for which the O VI absorption falls in the spectral region where S/N $\le$ 10. To get robust Voigt profile parameters we restrict ourselves to systems detected when the spectrum has S/N $>$ 10. The vertical tick mark on the right indicates the redshift at which the velocity difference from the QSO emission redshift ($z_{\rm em}$) is 5000 km s^{-1}. This defines the maximum redshift ($z_{\rm max}$) for each line of sight as given in column #4 of Table 1 & 4. This cut is applied to remove the O VI systems associated with the QSO or QSO neighborhood. Note that the two systems at $z_{\rm abs}$ = 2.0850 towards HE 1341−1020 and $z_{\rm abs}$ = 2.1660 towards PKS 1448−232 falling $\sim$ 5000 km s^{-1} from the respective emission redshifts have been included in the sample.

The maximum redshift path covered by the observations with S/N $>$ 10 is Δz = 7.62 or ΔX = 24.85. However, this should be treated as upper limits as line blanketing by Lyα lines reduce the available redshift path length.

3.1 Absorption line measurement techniques

3.1.1 Voigt profile fitting

We use standard Voigt profile fitting and apparent optical depth techniques to derive absorption line parameters. The Voigt profile fit provides best fitted values of the column density (N), velocity dispersion (b) and redshift (z) for each component. The absorption lines originating from individual species (H I, C IV and O VI) are fitted using all the detected transitions with minimum number of components required to get the reduced χ^2 close to 1. Whenever possible, we have tied the O VI and C IV components in redshift. However, most of the systems are best fitted by components with different sets of parameters for O VI and C IV. We use all the available Lyman series lines to extract N(H I). In this case also whenever possible component structure from metal lines were used to constrain the redshifts of individual H I components.

We also have independent Voigt profile decompositions for 51 O VI systems along 12 lines of sight (indicated by underlined QSO names in column #1 of Table 1) performed by Bergeron & Herbert-Fort (2005) using VPFIT [1] (Webb 1987; Rauch et al. 1992). In this case fits to H I, C IV and O VI absorption were performed independently without constraining the redshifts of any components. As the O VI absorption lines fall in the Lyα forest, some amount of subjectivity (wavelength range used, placement of components and number of components etc.,) is involved in the Voigt profile decomposition. However, the availability of decompositions derived using two independent procedures allow us to investigate the statistical influence of the fitting procedures.

In total we find 239 individual Voigt profile components for O VI (with 12.75 $\le$ log N(O VI)[cm^{-2}] $\le$ 14.49) and 318 components for C IV (with 11.58 $\le$ log N(O VI)[cm^{-2}] $\le$ 14.76). Total

---

[1] See http://www.ast.cam.ac.uk/~rfc/vpfit.html

Table 4. Details of additional O vi systems detected in the spectral range where continuum S/N ≤ 10

QSO	z_{em}	z_{min}	z_{max}	z_{sys}	log N(H i)	log N(O vi)	log N(C iv)	Class	Case	δ_{type}	δv(O vi) (km s^{-1})	δv(C iv) (km s^{-1})	$\lvert\Delta v$(O vi − C iv)$\rvert$ (km s^{-1})	Low Ions
Q 0122–380	2.190	1.995	2.137	1.9746	15.43± 0.16	14.72± 0.07	15.30±0.20	*bd*	B	−1	90.4	281.5	....	Yes
HE 2217–2818	2.414	1.963	2.357	1.9658	15.82± 0.57	14.95± 0.13	14.42±0.04	*bd*	A/B	0	328.3	171.1	42.66	Yes
Q 0453–423	2.658	2.014	2.597	2.0041	15.10± 0.09	14.26± 0.21	13.16±0.04	*bd*	B	+1	166.8	121.6	....	No
HE 2347–4342	2.871	2.311	2.807	2.1198	14.26± 0.04	14.42± 0.43	13.42±0.05	*bb*	A	+1	34.9	33.5	....	No
				2.2750	13.97± 0.13	14.59± 0.77	13.86±0.20	*bb*	A	−1	117.6	204.0	....	No
PKS 2126–158	3.280	2.520	3.208	2.4596	14.25± 0.05	14.30± 0.10	13.46±0.02	*bd*	B	0	48.4	41.8	1.55	No
				2.4855	15.11± 0.16	14.47± 0.11	12.61±0.06	*bb*	B	0	80.1	62.2	16.18	No

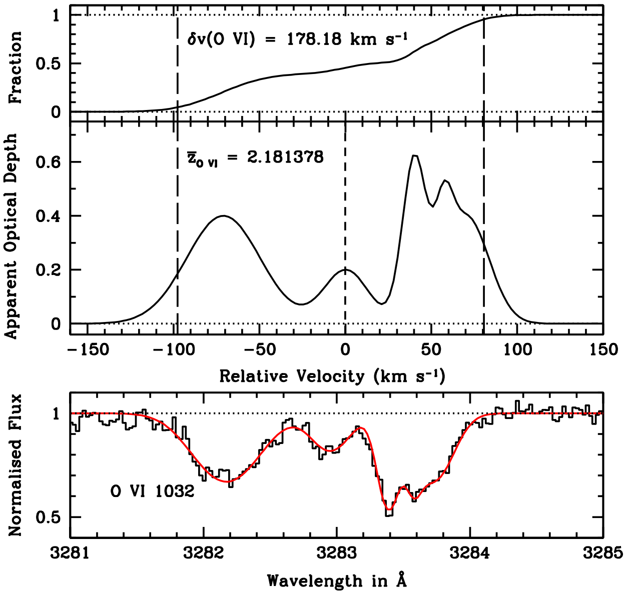

Figure 3. *Bottom* : The O vi λ1032 absorption profile of the system at z_{abs} = 2.1808 towards HE 2217−2818. The best fitted Voigt profile is overplotted. *Middle* : The apparent optical depth profile [$\tau_a(v)$] estimated from the best fitted Voigt profile is shown. The zero velocity corresponds to the optical depth weighted redshift $\bar{z}_{\rm O\,VI}$ = 2.181378. *Top* : Integration of the apparent optical depth. The line profile velocity width, δv, has been calculated as [v(95%) − v(5%)] where v(95%) and v(5%) are the velocities corresponding to 95 and 5% percentiles (vertical long dashed lines) of the apparent optical depth distribution.

column densities of H i, O vi and C iv are listed in Tables 1 and 4 in columns #6, #7 and #8, respectively. These are obtained by summing the column densities in individual Voigt profile components in a given system.

3.1.2 *Apparent optical depth (AOD)*

For each of these systems we have calculated the velocity width for O vi and C iv (when detected) absorption using AOD technique. Following Ledoux et al. (2006), the absorption velocity width, δv, has been calculated as [v(95%) − v(5%)], where v(95%) and v(9%) are the velocities corresponding to the 95 and 5 percent percentiles of the apparent optical depth distribution. Note this definition is slightly different from that used by Songaila (2006), who defined the velocity spread as the velocity range over which the optical depth is larger than some fraction of the peak optical depth. As pointed out by Songaila (2006), the velocity spread measurements are very sensitive to the velocity range over which the absorption is studied. Songaila (2006) used regions within 350 km s^{-1} either side of the peak optical depth. This in turn restricts the maximum measurable width to 700 km s^{-1}. In order to be consistent with our definition of a system, we consider here the velocity range covered by the Voigt profile components with no gap larger than 100 km s^{-1} (i.e. $v_{\rm link}$ ∼ 100 km s^{-1}).

The δv(O vi) is sometimes difficult to measure because of blending in the Lyα forest. Therefore, we introduce an index $\delta_{\rm type}$ (see column #11 of Tables 1 & 4) which takes the value 0, +1 and −1. The systems with $\delta_{\rm type}$ = 0 are the ones for which O vi absorption is well defined based on both the O vi lines. Systems with $\delta_{\rm type}$ = +1 and −1 are those for which the measured width should be considered as an upper and lower limit, respectively. There are 54 systems with $\delta_{\rm type}$ = 0.

We also calculate the first moment of the apparent optical depth distribution which gives us the optical depth weighted redshift for both C iv and O vi (i.e. $\bar{z}_{\rm C\,IV}$ and $\bar{z}_{\rm O\,VI}$). This allows us to calculate the velocity shift (called $|\Delta v$(O vi − C iv)$|$) between the O vi and C iv absorption originating from the same system.

Fig. 3 illustrates the way we measure δv. Bottom panel shows the observed O vi profile and the best fitted Voigt profile. In the middle panel we plot the AOD profile as a function of velocity. The top panel shows the integrated optical depth starting from a minimum velocity. The left and right vertical dashed lines mark the velocities at which the integrated optical depth is 5% and 95% of the total optical depth respectively. The velocity difference between these two lines gives δv. For clarity, the zero velocity is fixed at $\bar{z}_{\rm O\,VI}$ so that integrated optical depth is 50% at v = 0 km s^{-1}.

If both O vi and C iv absorption originate from the same gas with constant density and homogeneous ionization conditions then the velocity offset measured between $\bar{z}_{\rm O\,VI}$ and $\bar{z}_{\rm C\,IV}$ should be zero (i.e. $|\Delta v$(O vi − C iv)$|$ = 0). Any mismatch of the optical depth weighted redshifts between species could be interpreted as (a) relative line of sight velocity between the two species (as expected in the case of O vi originating from different interfaces like evaporating region, cooling front or shocked gas) or (b) ionization inhomogeneity along the line of sight. The measured δv(O vi), δv(C iv) and $|\Delta v$(O vi − C iv)$|$ in our sample are summarized in column #12, #13 and #14 of Tables 1 & 4, respectively.

3.2 Sub-samples of O vi systems

As O vi originates from a whole range of physical conditions and because of blending, the characteristics of the O vi absorption are difficult to extract. Hence, we build different subsamples depending on the issue we want to address.

The H i column density and b-parameter are very important for understanding the physical state of O vi gas (see e.g., Tripp et al. 2008). In particular, to investigate whether the gas is photoionized, we need to know N(H i) in individual O vi components. So we define “Case-A” systems as the ones where at least one of the Lyman series line is unsaturated. In principle these systems also enable us

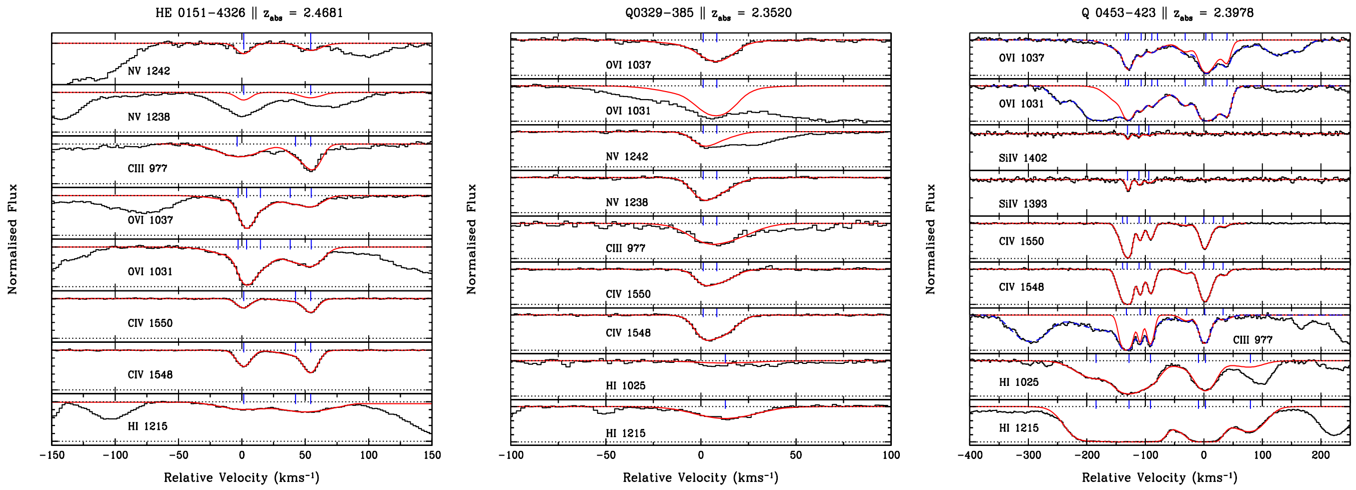

Figure 4. Examples of O vi systems where both lines in the doublet are unblended (left; *dd*), one of the line in the doublet is blended (middle; *bd*) and both lines in the doublet are partially blended (right; *bb*). The smooth curves are the best fitted Voigt profiles. The horizontal tick marks indicate the centroids of the individual components. The absorption redshift that defines the zero velocity and the name of the background QSO are indicated at the top of each panel.

to derive b-values for most of the H i components. There are 35 systems classified as "Case-A" systems in our sample. The systems shown in the left and middle panels of Fig. 4 are examples of "Case-A" systems. There are 10 systems where at least one H i absorption is unsaturated for some of the components. We call these systems at "Case-A/B". The right most panel in Fig. 4 is an example of such a case. In the remaining systems most of the H i absorption is saturated and Voigt profile measurements are uncertain. We call these systems "Case-B". We notice that several of the "Case-B" systems show absorption lines from low ionization species such as C ii, C iii, Si iii/Si iv etc. The information regarding the presence of low ions is also given in column #15 of Tables 1, 2 and 4. In total there are 46 systems where low ions are detected. Note that the C iii information is not available in our sample for $z \lesssim 2.2$.

We also classify the systems based on the presence of unblended O vi doublets. Out of 84 systems only 29 systems have both O vi lines unblended for which we are able to perform robust Voigt profile fits. We call this sample as "robust sample" as far as Voigt profile parameters are concerned (these are marked as "*dd*" in column #9 of Tables 1 and 4). An example of such a system is shown in the left panel of Fig. 4. In 30 other systems one of the O vi lines is blended (as in the middle panel of Fig. 4). Here the O vi fit relies mainly on the unblended line. We denote these systems as "*bd*" in column #9 of Tables 1 and 4. In the remaining 25 systems both lines are partially blended (as in the right panel of Fig. 4). In this case (referred to as "*bb*" in column #9 of Tables 1 and 4) we use part of the profiles of both O vi lines to fit the Voigt profiles. In most of these cases the additional absorption is treated as due to intervening Lyα absorption. Therefore, the Voigt profile parameters (number of components and b-values) are uncertain.

4 ANALYSIS BASED ON VOIGT PROFILE FIT

In this section we discuss the distributions of various parameters derived from our Voigt profile fits.

4.1 *b*-parameter distribution

The b-parameter derived from Voigt profile fit provides only an upper limit to the kinetic temperature of the gas. Thus, we do not attempt to constrain the physical state of the O vi gas using individual b-values, instead we draw some broad conclusions using the b-parameter distributions.

First, we compare our O vi b-parameter distribution for the 12 lines of sight with that of the Bergeron & Herbert-Fort (2005). The Kolmogorov-Smirnov (KS) test suggests that the two distributions are drawn from the same parent population with a 32% probability for the observed deviation in the cumulative distributions to occur by chance.

In the bottom panel of Fig. 5 we plot the b-parameter distributions measured in individual Voigt profile components for O vi (solid histogram) and C iv (dot-dashed histogram) in our full sample. The (red) dashed histogram gives the b(O vi) distribution in the robust components (i.e. from "*dd*" subsample). The O vi components arising from systems with S/N $\leq$ 10 (listed in Table 4) are not included here. Median values of b(O vi) = 13.8 km s^{-1} and b(C iv) = 10.1 km s^{-1} correspond to $T \sim 1.8 \times 10^5$ K and 7.4×10^4 K for O vi and C iv respectively in the case of pure thermal broadening. The temperature corresponding to median b(O vi) agrees well with $T \sim 2.1 \times 10^5$ K found by Simcoe et al. (2002). The median b-value of O vi components becomes 12.5 km s^{-1} if we restrict ourselves to the robust sample. In the case of pure photoionization heating the expected temperature (i.e. $T \sim 2 \times 10^4$ K) implies b(O vi) $\sim$ 5 km s^{-1}. The lowest b(O vi) measured (4.9±3.2 km s^{-1}) in our sample is consistent with this.

In the case of collisional ionization, the fraction of oxygen in O vi peaks around $T \sim (2-3) \times 10^5$ K, which corresponds to b(O vi) $\sim$ 14.4 km s^{-1}. This is very close to the median b(O vi)-value of our full sample. This is shown by the left vertical dashed line in Fig. 5. There are 52% (and 62% for the *dd* subsample) components having b-parameters less than 14.4 km s^{-1} suggesting photoionization (and/or non-equilibrium collisional ionization at high metallicities) is the dominant process in these systems. On the other hand, the O vi fraction will be less than 0.01 when $T \geq 6 \times 10^5$ K (see Gnat & Sternberg 2007), or b(O vi) $\gtrsim$ 25.5 km s^{-1} (second vertical line in Fig. 5). Therefore under the purely thermally broad-

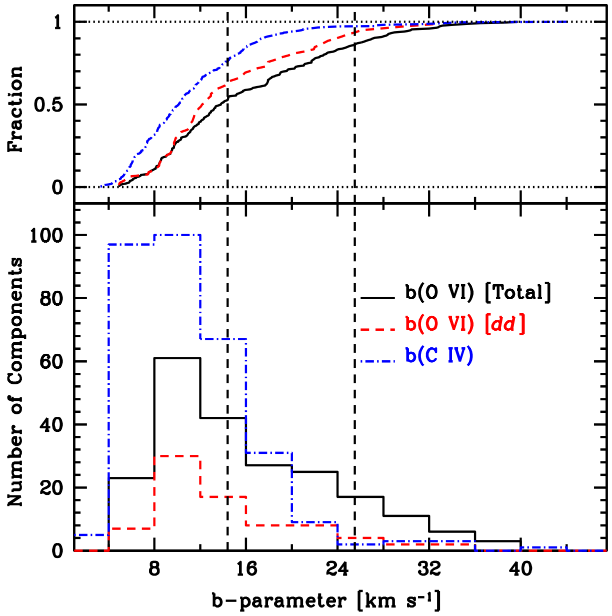

Figure 5. *Bottom* : Comparison of the b-parameter distributions of C IV (dot-dashed histogram) and O VI (solid histogram). The dashed histogram is for the O VI components originating from *dd* systems. The vertical dashed lines correspond to b(O VI) = 14.4 and 25.5 km s^{-1} respectively. *Top* : The cumulative b-parameter distributions of C IV, O VI (both total & *dd*) components are shown following the same line style as in the bottom panel.

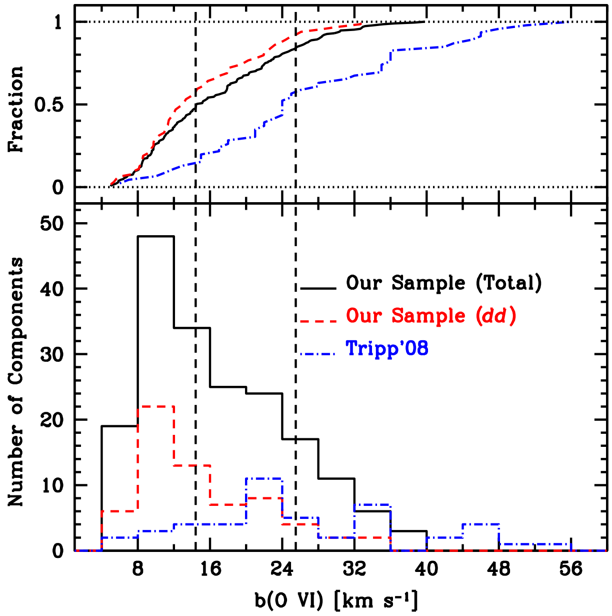

Figure 6. Comparison of the b-parameter distributions of O VI at high and low redshifts. The low-z sample is the STIS data sample of Tripp et al. (2008). Only those O VI components, originating from systems with log N(O VI)(cm^{-2}) > 13.6 (corresponding to a rest frame EW of ~ 50 mÅ) are considered here. The vertical dashed lines are as in Fig. 5. The overall b-distribution of our sample is significantly different from that of the low-z sample as can be seen from the cumulative distributions plotted in the top panel with the same line style as in the bottom panel.

ened case one does not expect the O VI b-parameter to be higher than this unless the metallicity and/or $N(H)$ is very high. These systems will also have broad and shallow associated Lyα. We find 14% (and 8% for the *dd* subsample) of the components having b-values higher than this. Most of these high b components in our sample are part of blends where the O VI profile is decomposed into multiple Voigt profile components. Isolated O VI components with b(O VI) > 25 km s^{-1} are very rare. Note that very few such isolated broad O VI components together with broad albeit shallow Lyα absorption are detected at low-z (see e.g., Savage et al. 2010, 2011). These are interpreted as collisionally ionized gas with $T \sim 10^6$ K. The non-detection of such systems in our sample may be attributed to the bias introduced by line blanketing and blending due to the Lyα forest absorption.

The temperature for which the ionization fraction of C IV peaks under collisional ionization equilibrium is ~ 1.1×10^5 K, or b(C IV) = 12.40 km s^{-1}. Sixty seven percent of the C IV components have b-parameter less than this suggesting that a considerable fraction of C IV originates either from photoionized gas or from non-equilibrium cooling gas with high metallicity (i.e. $Z \sim 1.0\ Z_\odot$). It is apparent from Fig. 5 that the b-parameter distribution is wider in case of O VI compared to C IV. This is evident in the cumulative distributions plotted in the top panel. The KS-test indicates that the two distributions are drawn from significantly different populations with the probability of this difference occurring by chance being less than 0.1%. Ideally one would expect b(C IV) ≥ b(O VI) if C IV and O VI trace the same gaseous phase. Our finding is consistent with O VI and C IV originating from different phases of the gas associated with the absorption system (see also, Simcoe et al. 2002; Bergeron & Herbert-Fort 2005).

Next we compare the b(O VI) distribution in our sample with the low-z sample of Tripp et al. (2008) obtained using the Space Telescope Imaging Spectrograph (STIS) on board *HST*. The spectral resolution of STIS data is ~ 7 km s^{-1}, very much similar to the one used here but the STIS spectra are slightly under-sampled. Even though the S/N of STIS spectra are typically a factor of two lower than those of our UVES data, the contamination by intervening H I absorption is less severe in the low-z sample. In the bottom panel of Fig. 6 we show the two O VI b-distributions. We restrict the comparison to systems with log N(O VI) (cm^{-2}) > 13.6 which is the completeness limit of the STIS sample. The median b-values for the low and high-z O VI components are 24.0 and 14.6 km s^{-1} (13.2 km s^{-1} for the *dd* subsample), respectively. It is interesting to note that almost 87% of the low redshift b-parameters are consistent with the temperature expected from collisional ionization, i.e., b(O VI) > 14.4 km s^{-1} (first dashed vertical line), only 53% (44% for the *dd* subsample) of the high redshift components satisfy this.

Almost 43% of the low redshift components are consistent with b > 25.5 km s^{-1} (second dashed vertical line). In our high redshift sample, only 16% (9% for the *dd* subsample) components show b-value greater than 25.5 km s^{-1}. The overall b-distribution of our sample is significantly different from that of the low-z sample as can be seen from the cumulative distributions plotted in the top panel of the Fig. 6. A two sided KS-test gives a maximum departure between the two distributions, D = 0.41 with a probability, P = 3.9×10^{-6} that the two samples are drawn from the same parent population. The difference is even more when we compare the low-z sample to our *dd* subsample as can be seen from the cumulative distributions.

In summary, we find that at high redshift, the b-parameter distributions of C IV and O VI are significantly different with O VI absorption being wider than C IV, suggesting that the two species

Table 5. Results of decomposition of thermal and non-thermal contributions to the line broadening

QSO	z_{sys}	v_{rel} (km s^{-1})	b(H i) (km s^{-1})	b(O vi) (km s^{-1})	b(C iv) (km s^{-1})	log N (cm^{-2}) H i	log N (cm^{-2}) O vi	log N (cm^{-2}) C iv	b_{nt} (km s^{-1})	log T (T in K)	log T_{max}[2] (T_{max} in K)
PKS1448-232	2.1099	−4.7	14.2	8.1	7.3	13.05	14.28	13.11	7.5 (6.3)	3.94 (3.99)	≤4.09
PKS 0237–23	1.9878[1]	+0.4	20.6	9.5	...	13.64	13.41	...	8.2	4.33	≤4.41
PKS 0237–23	2.0108[1]	−3.8	31.3	9.4	...	14.31	13.15	...	5.4	4.76	≤4.77
Q 0329–385	2.0764	+4.9	19.7	7.9	6.2	13.64	13.26	13.21	6.4 (2.6)	4.32 (4.36)	≤4.37
Q 0329–385	2.2489[1]	−50.3	18.6	8.2	...	12.76	13.68	...	7.0	4.26	≤4.32
Q 0329–385	2.2489[1]	−19.4	10.1	10.3	...	11.95	13.47	...	...	....	≤3.79
Q 0329–385	2.2489[1]	− 3.1	33.1	21.9	...	13.11	13.76	...	20.9	4.60	≤4.82
Q 0329–385	2.2489[1]	+43.4	24.7	12.1	...	13.10	13.64	...	10.7	4.48	≤4.57
Q 0329–385	2.3139	+4.0	38.6	11.5	4.3	14.02	13.16	11.79	6.5 (...)	4.94 (...)	≤4.96
Q 0329–385	2.3139	+34.8	16.9	8.8	5.8	13.23	12.75	12.21	8.0 (3.3)	4.13 (4.22)	≤4.24
Q 0329–385	2.3639	−46.3	27.8	15.3	9.2	14.40	13.37	11.86	14.1 (4.7)	4.54 (4.66)	≤4.67
Q 0329–385	2.3639	−4.1	19.0	8.7	9.1	13.91	13.52	12.25	7.5 (7.6)	4.27 (4.26)	≤4.34
HE 1347–2457	2.3327[1]	+3.2	23.5	18.5	...	13.78	13.26	...	18.1	4.13	≤4.52
HE 1347–2457	2.3422[1]	+10.8	18.3	9.9	...	14.40	12.95	...	9.1	4.18	≤4.31
Q 0453–423	2.5371[1]	−26.3	38.7	10.3	...	13.48	13.05	...	3.6	4.95	≤4.96
Q 0453–423	2.5371[1]	−1.6	28.5	11.7	...	14.62	13.17	...	9.6	4.64	≤4.69
PKS 0329–255	2.5687	−3.9	30.0	10.1	6.1	14.62	13.12	12.15	7.0 (...)	4.71 (...)	≤4.74
PKS 0329–255	2.5687	+14.2	29.9	13.8	20.8	14.25	13.35	12.27	12.0 (19.8)	4.66 (4.48)	≤4.73
HE 0151–4326	2.5053	+42.6	28.0	21.7	10.5	14.71	13.52	12.10	21.2 (7.0)	4.31 (4.65)	≤4.68
HE 2217-2818	2.0748	+64.4	29.0	12.6	...	14.12	14.32	...	10.6	4.64	≤4.71

Table Notes – [1]Components from "O vi only" systems. [2]Calculated from b(H i) assuming pure thermal broadening.
Values in the parenthesis are calculated using b(H i) – b(C iv) pairs.

trace different phases of the absorbing gas. The b(O vi) distribution at high-z is very different from that at low-z as measured by Tripp et al. (2008). Recently Fox (2011) has drawn a similar conclusion using the high-z Voigt profile fitting results of Bergeron & Herbert-Fort (2005).

4.2 Thermal and non-thermal contributions to b-parameters

In the previous section we find that on an average b-parameters of O vi measured at low-z are higher than that measured at high-z. To explore this further we use a subsample of O vi absorbers where O vi and H i absorption are well aligned. In general the line width of any species can be decomposed into thermal (b_{th}) and non-thermal (b_{nt}) parts, i.e. $b^2 = b_{th}^2 + b_{nt}^2$. For species located in the same physical region, the non-thermal part is supposed to be identical whereas the thermal part scales inversely with the mass of the ion.

Line saturation in the case of Lyα and blending with H i lines in the case of O vi make the robust estimation of b-parameters for H i and O vi difficult in our sample. In addition we need to ensure that there is a good alignment between O vi and H i absorption. Hence we select systems using the following two criteria : (1) The component structure of H i is well defined and one of the available Lyman series lines is unsaturated (i.e. "Class-A" absorbers as defined in Table 1). (2) The O vi profiles are well defined and the velocity offset between H i and O vi absorption centroids are consistent with zero within 3σ uncertainty. We also avoid systems with low ion absorption lines as H i seems to be predominantly associated with the low-ionization phase when these species are present (see section 6). Thus by using these selection criteria we minimize the probability that these absorbers have a multiphase structure.

We find only 13 systems with 19 Voigt profile components (identified by vertical dashed lines in Fig. 7) satisfying the conditions listed above. This is only ~ 15% (i.e. 13 out of 84 systems) of our full sample. There are 6 systems showing only O vi and H i absorption (i.e. "O vi only" systems). In the remaining 7 systems both O vi and C iv absorption are seen. In 6 of them O vi and C iv components are remarkably aligned. In these cases we estimate the temperature and b_{nt} using both b(H i)–b(O vi) and b(H i)–b(C iv) pairs. Only in the case of the z_{abs}= 2.0748 system towards HE 2217–2818, the corresponding C iv component is ~ 4.2 km s^{-1} away from the O vi component and hence it is not used in our analysis.

The results of the decomposition in thermal and non-thermal broadening are summarized in Table 5. Columns #1, #2 and #3 list, respectively, the QSO name, system redshift (z_{sys}) and the velocity of the component (v_{rel}) with respect to the systemic redshift. Columns #4, #5 and #6 give b-values of H i, O vi and C iv components, respectively. The corresponding column densities are given in columns #7, #8 and #9 respectively. The non-thermal contribution to the broadening and the estimated temperature are listed in columns #10 and #11, respectively. The values in parenthesis are calculated using b(H i)–b(C iv) pairs. Column #12 lists the upper limits on the temperature as calculated from b(H i) assuming pure thermal broadening. It can be seen from the table that the temperatures estimated from the b(H i)–b(C iv) pairs are consistent with those derived from the b(H i)–b(O vi) pairs, whereas b(C iv) gives slightly lower b_{nt} compared to that obtained using b(O vi).

In Fig. 8 we show the distribution of b_{nt} (top) and temperature (bottom) as calculated from the b(H i)–b(O vi) pairs. The solid histogram shows the results by Tripp et al. (2008) for the low-z well aligned O vi absorbers for comparison. The values of non-thermal velocity in our sample are found to be in the range 3.6 ≤ b_{nt} ≤ 21.2 km s^{-1} with a median value of 8.2 km s^{-1}. The median value of b_{nt} for the Tripp et al. (2008) sample is ~ 20.0 km s^{-1}. From the top panel of Fig. 8 it is apparent that the b_{nt} distributions at high and low-z are significantly different. This is confirmed by a two sided KS test with a probability that the two distributions differ much greater than 99.9%.

The median value of the temperature distribution in both high and low redshift samples is found to be ~ 3×10^4 K. The KS test shows that the temperature distribution of low-z sample is not significantly different from high-z sample (~ 38% probability that the difference is occuring by chance). It is interesting to note that

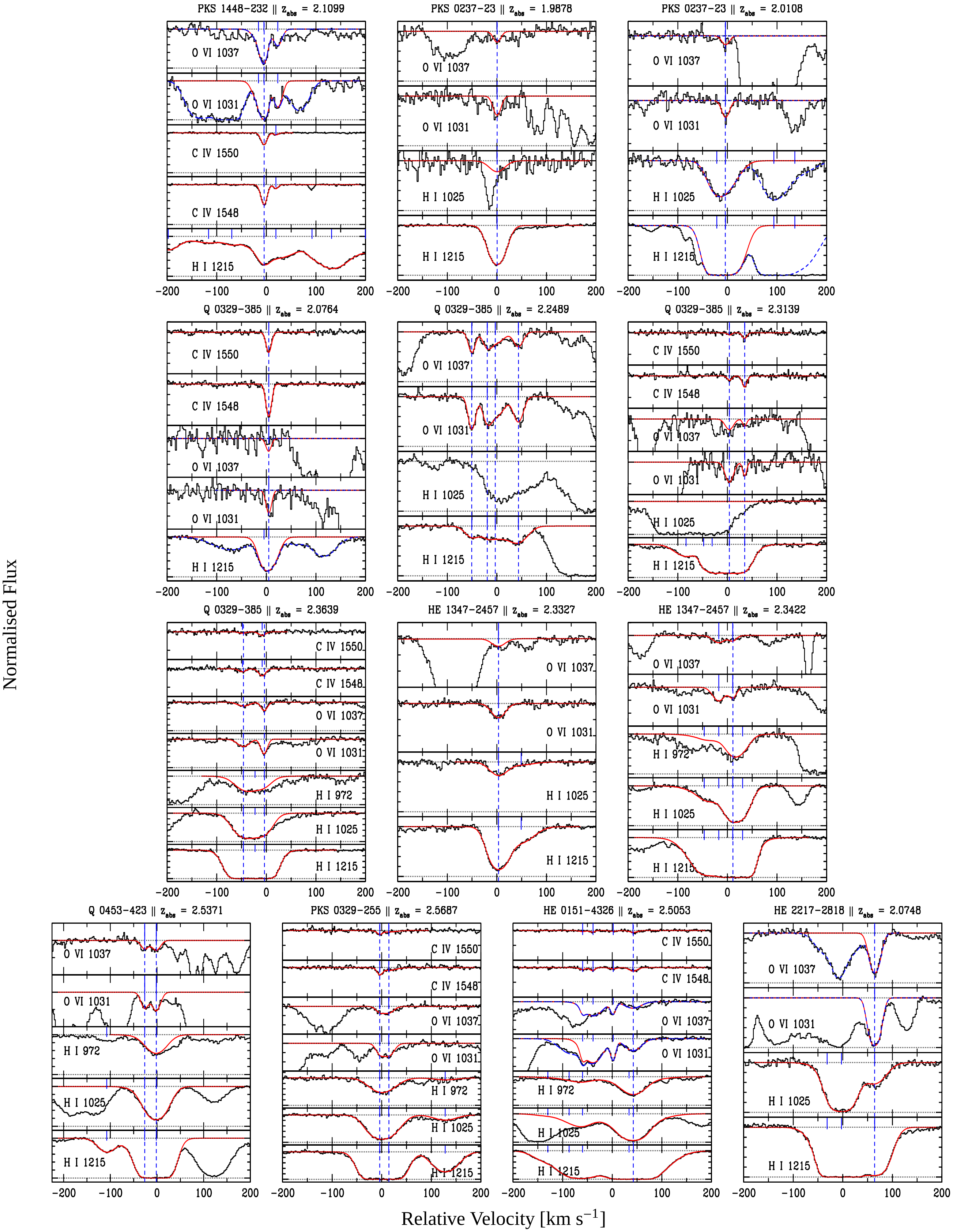

Figure 7. Velocity plots of the 13 well aligned systems that are used to measure temperature and turbulent motion of the absorbing gas. The best fitted Voigt profiles are over-plotted on the observed data. The vertical tick marks show the positions of individual components. The vertical dashed lines mark the components used for this study. The occasional dashed curves over-plotted on the data show the contamination from other intervening absorption. The absorption redshift that defines the zero velocity and the name of the background QSO are indicated at the top of each panel.

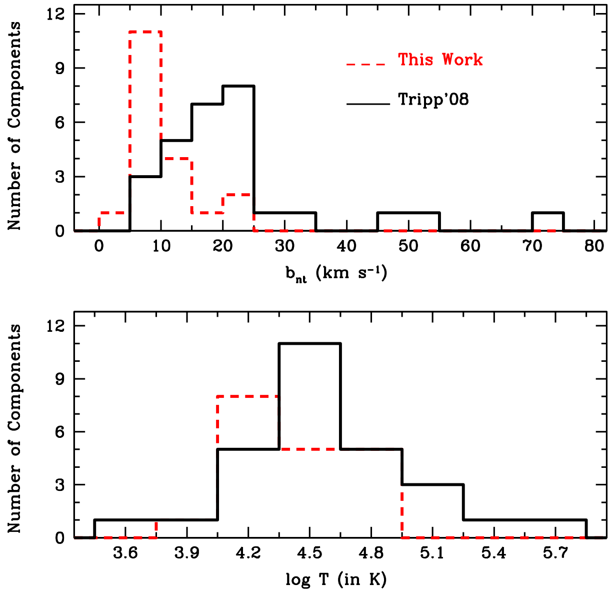

Figure 8. Distributions of temperature (lower panel) and turbulent velocity (upper panel) in the well aligned sample are shown in dashed histogram. The solid histogram in both panels shows the corresponding distribution at low-*z* as derived by Tripp et al. (2008).

Table 6. Results of Spearman rank correlation analysis

Observable-1	Observable-2	This Work		Tripp et al. (2008)	
		ρ_s	ρ_s/σ	ρ_s	ρ_s/σ
b_{nt}(O VI)	N(O VI)	+0.41	+1.7	+0.31	+1.6
b_{nt}(O VI)	N(H I)	+0.21	+0.9	+0.07	+0.4
b_{nt}(O VI)	b(O VI)	+0.78	+3.3	+0.99	+5.2
b_{nt}(O VI)	b(H I)	−0.05	−0.2	+0.56	+2.9
log T(O VI)	b(O VI)	+0.30	+1.3	+0.21	+1.1
log T(O VI)	b(H I)	+0.92	+3.9	+0.83	+4.3

while none of the components has temperature log $T \geq 5.3$ (which would favor collisional ionization for O VI), 42% of the components (i.e. 8 out of 19 components) show $4.6 \leq \log T \leq 5.0$, which is warmer than the temperatures expected in photoionization equilibrium. These higher temperatures can be obtained in a rapidly cooling over-ionized gas that was shock heated through mechanical processes such as galactic winds. We thus compare the observed N(O VI)/N(H I) in these well aligned components with the non-equilibrium collisional ionization models of Gnat & Sternberg (2007) assuming the temperature derived from b(H I) (given in column #12 of Table 5) and find that the observed ratios can not be reproduced by these models (even when we use maximum gas temperature) for gas phase metallicity less than solar. Thus it seems that the ionization state is probably maintained by the UV background radiation which is expected to dominate when $T \leq 10^5$ K (see Fig. 9 of Muzahid et al. 2011).

In Table 6 we summarize the Spearman rank correlation analysis to search for possible correlations between b_{nt}, log T and other observables of O VI absorbers discussed here as well as in Tripp et al. (2008). In all the correlation analysis presented in this paper, the correlation coefficient and its significance are denoted by ρ_s and ρ_s/σ, respectively. As expected, b_{nt} and log T are strongly correlated to b(O VI) and b(H I), respectively, with a very high correlation coefficient ($\gtrsim 0.8$) and at $> 3\sigma$ significance level in both samples. A weak correlation (at $< 2\sigma$ level) is seen between b_{nt} and N(O VI), both at high and low redshift. Recent simulations of Cen & Chisari (2011) suggest such a trend of higher non-thermal contribution at higher N(O VI). On the other hand Oppenheimer & Davé (2009) have introduced density dependent turbulence in their simulations in order to reproduce the equivalent width distribution and the $b - N$ correlation of low-z O VI absorbers. The lack of strong correlation between b_{nt} and N(O VI) or N(H I) in our sample suggesting that this density dependence of turbulence may be weak at high-z.

Table 7. Summary of power law index measurements for C IV CDDF

Redshift	> log N(C IV)	$\beta_{\rm C\,IV}$		References
		Systems	Components	
1.9–3.1	12.6	1.6±0.1	1.9±0.1	1
1.9–3.1	13.0	1.7±0.1	2.0±0.1	1
	13.4	1.64±0.10	....	2
2.9–3.5	13.0	1.8±0.1	....	3
	13.0	1.71±0.07	....	4
	12.3	1.44±0.05	....	5
		1.6	1.8	6
< 1.0	13.2	$1.50^{+0.17}_{-0.19}$	...	7

References:– (1) This work; (2) Petitjean & Bergeron (1994); (3) Songaila (2001); (4) D'Odorico et al. (2010); (5) Ellison et al. (2000); (6) Boksenberg et al. (2003); (7) Cooksey et al. (2010)

4.3 Column density distributions

In this section, we study the column density distribution functions (CDDF) of C IV and O VI systems in our sample. We use the usual parametrization of the column density distribution function, i.e.,

$$f(N)dN = BN^{-\beta}dN, \tag{1}$$

where, $f(N)$ is the number of systems/components per unit column density interval per unit redshift path length defined as,

$$dX = (1+z)^2[\Omega_\Lambda + \Omega_{\rm m}(1+z)^3]^{-1/2}dz. \tag{2}$$

We use the maximum likelihood method to estimate the power law index, β. The column density distribution functions of O VI systems (top) and components (bottom) are shown in the left panel of Fig. 9. The (blue) squares in the bottom panel correspond to the O VI component CDDF derived from the fits by Bergeron & Herbert-Fort (2005) for only 12 sight lines. It is in good agreement with our results based on the full sample. As mentioned above, we cover a redshift path (Δz) of 7.62 (and ΔX = 24.85) with the full sample where the S/N is > 10 per pixel. This figure shows that our survey is not severely affected by incompleteness for log N(O VI) > 13.7 as indicated by the vertical dotted line.

A maximum likelihood fit to our data gives a power law index of $\beta_{\rm O\,VI} = 1.9 \pm 0.1$ for O VI systems and $\beta_{\rm O\,VI} = 2.4 \pm 0.2$ for O VI components for log N(O VI) > 13.7 . We would like to mention that in the subsample *dd* where both lines in the doublet are unblended, we find $\beta_{\rm O\,VI} = 2.2 \pm 0.3$ for systems and $\beta_{\rm O\,VI} = 2.7 \pm 0.4$ for components . These values are somewhat steeper than, albeit consistent with, the full sample within the measurement uncertainties. For a sample of low redshift ($z < 0.15$) O VI absorbers with Lyα rest frame equivalent width ($W_{\rm Ly\alpha}$) ≥ 80 mÅ, Danforth & Shull (2005) found $\beta_{\rm O\,VI} = 2.2 \pm 0.1$ for the components. In a latter paper studying an extended sample of O VI absorbers, Danforth & Shull (2008)

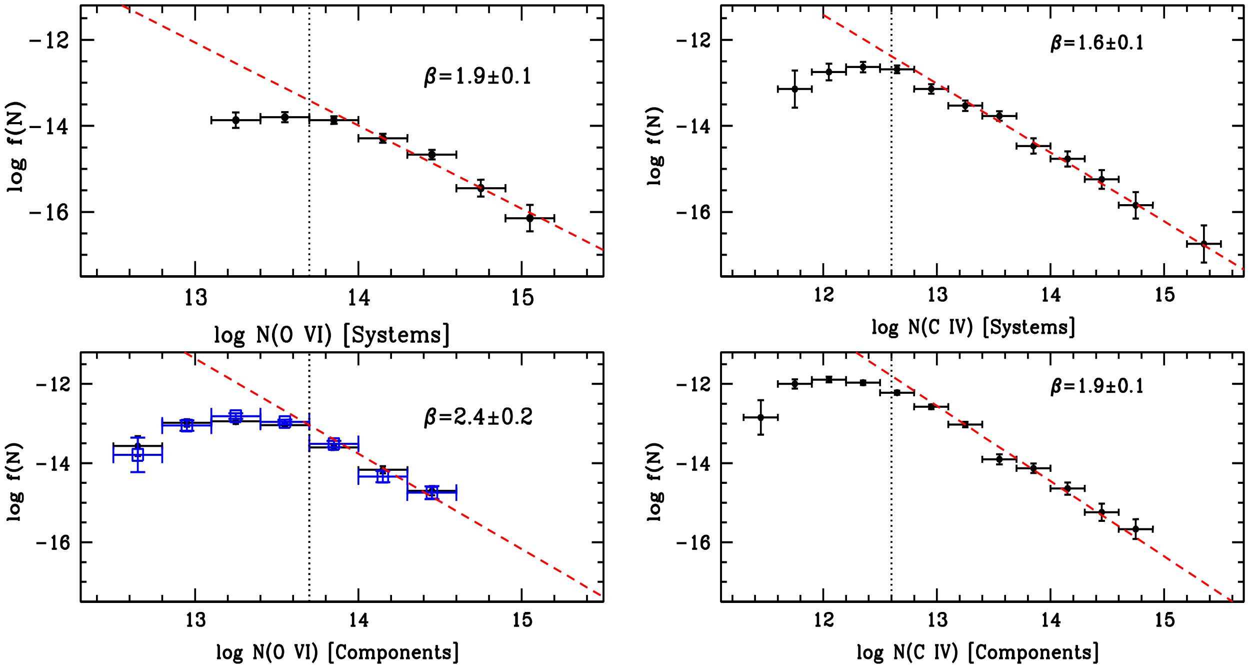

Figure 9. *Left:* Column density distribution functions of O VI systems (upper panel) and O VI components (lower panel). The *y*-axis is the number of systems/components per column density interval per unit redshift path length. The bin size along the column density axis is $10^{0.3}$cm^{-2} and the 1σ error bars in the y-axis are calculated using Poisson statistics. The (blue) squares are taken from Bergeron & Herbert-Fort (2005). The dashed straight lines are power laws of the form $f(N) = BN^{-\beta}$. The power law indices, β, are obtained using the maximum likelihood method where no binning is involved. Vertical dotted lines show the column density above which our sample is complete. *Right:* Same as left but for C IV.

found $\beta_{\rm O\,VI}$ to be 1.98±0.11. In addition, we have performed a maximum likelihood analysis on the low-*z* sample of Tripp et al. (2008) and found $\beta_{\rm O\,VI} = 2.3 \pm 0.2$ for components and 2.0±0.2 for systems for log N(O VI) > 13.7. Therefore the $\beta_{\rm O\,VI}$ measurements at low-*z* are consistent with our estimations.

The right panels of Fig. 9 show the C IV column density distribution function for components (lower panel) and systems (upper panel). Incompleteness limit is clearly log N(C IV)(cm^{-2}) ≥ 12.6 as shown in the figure by a vertical dotted line. Using maximum likelihood analysis, we find, $\beta_{\rm C\,IV}$, to be 1.6±0.1 for systems and 1.9±0.1 for components for log N(C IV) > 12.6. Our results are consistent with the earlier findings (Petitjean & Bergeron 1994; Songaila 2001; D'Odorico et al. 2010) within 1σ uncertainty when we use similar column density cutoff (i.e. log N(C IV) > 13.0; see Table 7).

4.4 O VI and C IV cosmological densities

In this section we compute the contribution of O VI and C IV absorbers to the baryon density using our column density estimates. The cosmic density of the O VI absorbers can be expressed as :

$$\Omega_{\rm O\,VI} = \left(\frac{H_0\, m_{\rm O}}{c\, \rho_{\rm cr}}\right)\left(\frac{\sum_{\rm i} N_{\rm i}({\rm O\,VI})}{\Delta X}\right), \quad (3)$$

with an associated fractional variance (as proposed by Storrie-Lombardi et al. 1996):

$$\left(\frac{\delta\Omega_{\rm O\,VI}}{\Omega_{\rm O\,VI}}\right)^2 = \frac{\sum_{\rm i}[N_{\rm i}({\rm O\,VI})]^2}{[\sum_{\rm i} N_{\rm i}({\rm O\,VI})]^2}\,, \quad (4)$$

where H_0 is the Hubble constant, $m_{\rm O}$ is the atomic mass of oxygen, ΔX and $\rho_{\rm cr}$ are the total redshift path and the current critical density, respectively. We find $\Omega_{\rm O\,VI} = (1.0 \pm 0.2) \times 10^{-7}$ for log N(O VI) > 13.7. If we include the LLS in our calculation then $\Omega_{\rm O\,VI} = (1.3 \pm 0.3) \times 10^{-7}$ for the same column density cutoff. Using the column densities of 12 intervening systems listed in Table 2 of Simcoe et al. (2002) we calculate $\Omega_{\rm O\,VI}$ for their sample. For their uncorrected redshift path (i.e. $\Delta X = 6.9$), $\Omega_{\rm O\,VI}$ turns out to be $(1.2\pm0.5)\times10^{-7}$ for log$N$(O VI) > 13.7 which is in good agreement with what we find here. For the 12 lines of sight our estimated value of $\Omega_{\rm O\,VI}$ is in excellent agreement with Bergeron & Herbert-Fort (2005).

It is also possible to calculate the fractional contribution to the cosmological density of the baryons associated with the O VI phase, provided the ionization fraction of O VI ($f_{\rm O\,VI}$) and the metallicity (Z) of the gas are known, viz.,

$$\Omega^{\rm O\,VI}_{\rm IGM} = \left(\frac{H_0\, \mu m_{\rm H}}{c\rho_{\rm cr}}\right)\left(\frac{1}{f_{\rm O\,VI} Z({\rm O/H})_\odot}\right)\left(\frac{\sum_{\rm i} N_{\rm i}({\rm O\,VI})}{\Delta X}\right). \quad (5)$$

Where $\mu = 1.3$ is the mean atomic weight and $m_{\rm H}$ is the mass of the hydrogen atom. For log N(O VI) > 13.7 the value of $\Omega^{\rm O\,VI}_{\rm IGM}$ is : $\Omega^{\rm O\,VI}_{\rm IGM} = 0.0011[(h/0.71)(Z/0.1Z_\odot)(f_{\rm O\,VI}/0.2)]^{-1}$. For $f_{\rm O\,VI} = 0.2$ and $Z = 0.1Z_\odot$, we get $\Omega^{\rm O\,VI}_{\rm IGM}/\Omega_{\rm b} = 0.028$ i.e. O VI absorbers contribute 2.8% to the total baryon density at redshift $z \sim 2.3$. For a more typical IGM metallicity of $Z = 0.01Z_\odot$ this contribution can go up to ∼ 30%. At low redshift ($z < 0.4$) Danforth & Shull (2008) derived $\Omega^{\rm O\,VI}_{\rm IGM}/\Omega_{\rm b} = 0.073 \pm 0.008$ down to log N(O VI) = 13.4 and 0.086 ± 0.008 down to log N(O VI) = 13.0 (for $f_{\rm O\,VI} = 0.2$ and $Z = 0.1Z_\odot$).

Using Eqn. (3) for log N(C IV) > 12.6, we find $\Omega_{\rm C\,IV} = (2.4 \pm 0.6) \times 10^{-8}$ without including Lyman limit systems. Inclusion of

Table 8. Summary of $\Omega_{\rm C\,IV}$ measurements

Redshift	$\Omega_{\rm C\,IV} \times (10^{-8})$	References
< 1.0	6±1	1
1.9–3.1	5.3±2.2	2
2.0–2.5	6.83	3
2.0–2.5	5.0±1.0	4
~ 2.2	7.5±2.2	5
~ 2.5	3.8±0.7	6
2.5–3.0	4.79	3
2.5–3.0	3.2±0.7	4
5.3–6.0	$\lesssim 1.3$	7
~ 5.8	0.44±0.26	8

References:– (1) Cooksey et al. (2010); (2) This work; (3) Songaila (2001); (4) D'Odorico et al. (2010); (5) Scannapieco et al. (2006); (6) Boksenberg et al. (2003); (7) Becker et al. (2009); (8) Ryan-Weber et al. (2009)

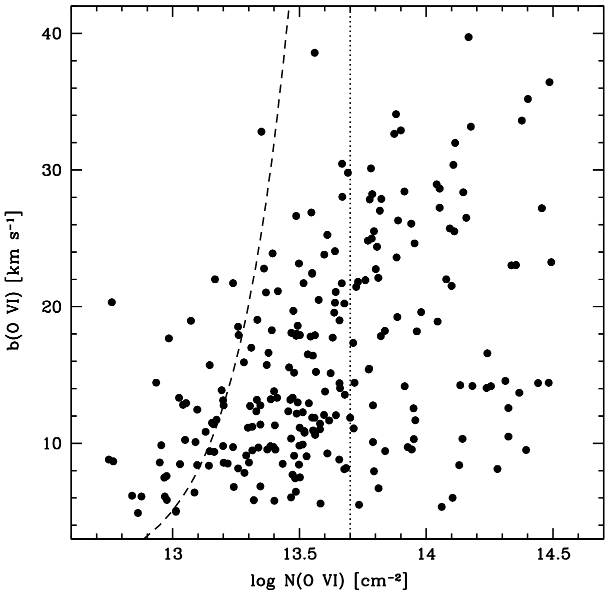

Figure 10. N(O vi) against b(O vi) measured in individual components. The short dashed curve and the dotted line show the 5σ detection threshold and the N(O vi) limit for the sample completeness respectively.

LLS increases the value up to $(5.3\pm2.1)\times10^{-8}$. This value compares well with the previous estimations (Songaila 2001; Simcoe et al. 2004; Scannapieco et al. 2006; D'Odorico et al. 2010) for a similar redshift range as can be seen from Table 8. For completeness, the recent $\Omega_{\rm C\,IV}$ measurements for $z > 5$ are also summarized in this table.

4.5 $b - N$ correlation

A correlation between column density and b-parameter of O vi components has been predicted by theoretical studies of hot ionized gas (see Edgar & Chevalier 1986; Heckman et al. 2002) as a natural consequence of radiatively cooling hot gas passing through a coronal regime. Heckman et al. (2002) have shown that such a correlation exists in a wide variety of astrophysical environments (such as Galactic disk, halo, High Velocity Cloud (HVC), Large Magellanic Cloud (LMC), Small Magellanic Cloud (SMC), starburst galaxies, IGM etc.). These authors have also shown that the relationship between the log N(O vi) and log b is linear for the broad lines (i.e. b(O vi) > 40 km s^{-1}) but rolls over and steepens for the narrower lines. Danforth et al. (2006), Tripp et al. (2008) on the other hand, report no convincing evidence of such correlation for the low redshift intergalactic O vi absorbers. Lehner et al. (2006) revisited the Heckman et al. (2002) model and found that their sample of O vi absorbers is consistent with the model but the observed N(Ne viii) is much less than the model prediction.

Table 9. Results of correlation analysis between N(O vi) and b(O vi)

Sample	> log N(O vi)	Components	ρ_s	ρ_s/σ
Total	13.7	82	0.05	0.4
dd	13.7	19	−0.36	−1.5
bd	13.7	22	0.17	0.8
bb	13.7	41	0.24	1.5

In Fig. 10 we plot the O vi b-values against column densities in individual components for our full sample. The dashed curve shows the 5σ detection threshold of our data assuming S/N ~ 10 in the forest. The limiting equivalent width for a given b-value has been calculated using the prescription by Hellsten et al. (1998). This limiting equivalent width is then converted to a column density assuming the optically thin case. The vertical dotted line at log N(O vi) = 13.7 shows our sample completeness (see section 4.3). For log N(O vi) > 13.7 the $b - N$ space is uniformly populated by the data points indicating the lack of any significant correlation. The results of Spearman rank correlation analysis performed between N(O vi) and b(O vi) in our full sample and various subsamples are given in Table 9. No statistically significant correlation is found in any of these cases when appropriate column density limit (i.e. log N(O vi) > 13.7) is considered.

5 ANALYSIS BASED ON APPARENT OPTICAL DEPTH

In this section, we study the line kinematics of O vi and C iv absorption using the line spread (δv) and the velocity shift (Δv) between the C iv and O vi optical depth weighted redshifts defined in section 3.1.2. For most of the discussions presented below, unless otherwise stated, we restrict ourselves to the $\delta_{\rm type} = 0$ subsample defined in Table 1.

5.1 Line spread (δv) distribution

In the left panel of Fig. 11, we show the δv distribution of O vi systems (solid histogram) and C iv systems (dashed histogram, including all C iv systems). The median value of δv(O vi) is 66 km s^{-1} and the maximum observed value is 340 km s^{-1}. The median value of δv(C iv) is 58 km s^{-1}. The δv distributions of O vi and C iv, appear fairly similar except in the first velocity bin. If the latter is considered, the KS-test gives a probability of 0.1% that the two distributions are drawn from the same population (see top panel in Fig. 11). However if it is excluded, then the KS-test shows only a ~ 52% probability that the two distributions differ. The lack of O vi systems with δv(O vi) < 40 km s^{-1} could be related to the difficulty in detecting narrow systems in the Lyα forest.

In the right panel of Fig. 11, we plot the C iv line spread against that of O vi. The (red) filled circles are for systems with $\delta_{\rm type} = 0$. A strong correlation between δv(C iv) and δv(O vi) is apparent from the figure. The Spearman rank correlation coefficient for the robust measurements is ~ 0.81 with ~ 5.3σ significance. The slope (0.81 ± 0.11) and the intercept (−8.60 ± 9.17) of the best

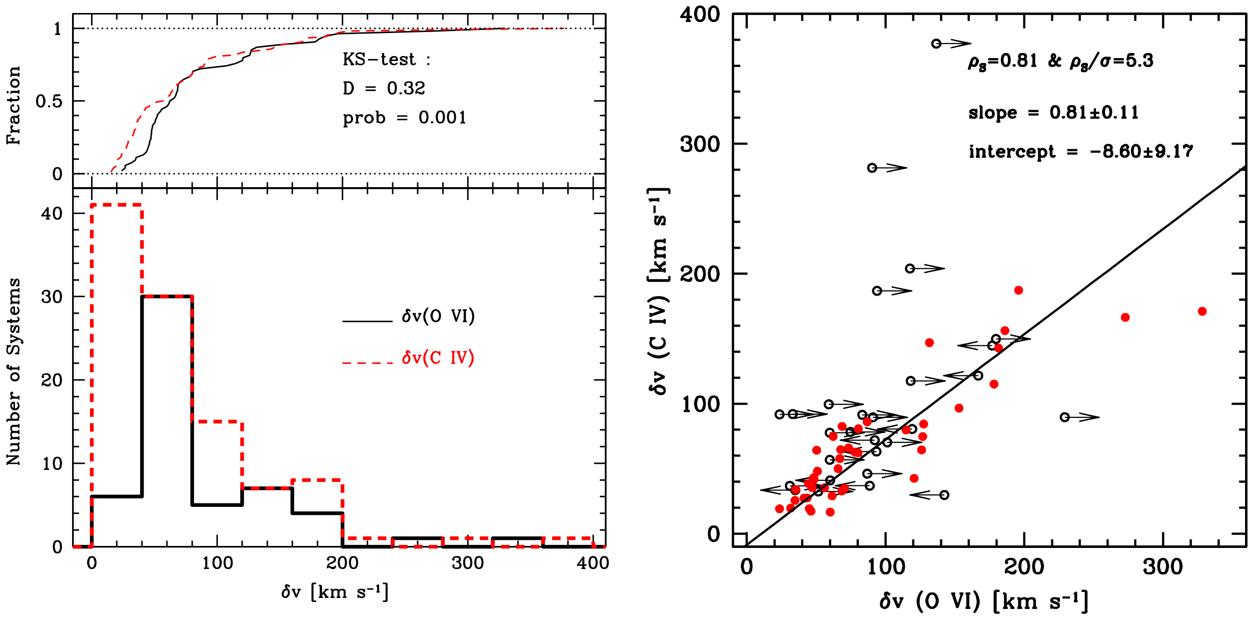

Figure 11. *Left :* δv distributions of O VI (solid histogram) and C IV (dashed histogram) systems. Corresponding cumulative distributions are plotted in the upper panel. *Right :* δv(C IV) versus δv(O VI). The (red) solid circles are for the systems with $\delta_{\rm type}$ = 0 whereas the arrows indicate systems with $\delta_{\rm type}$ = ±1. The straight line shows the least square fit to the data for systems with $\delta_{\rm type}$ = 0.

fitted straight line to the (red) solid circles indicates that the spread of C IV absorption is systematically smaller than that of O VI for a given δv(O VI).

There are three O VI (top panel of Fig. 12) and three C IV systems (bottom panel of Fig. 12) with $\delta v > 200$ km s^{-1}. These large velocity spreads could be related to either (a) large scale winds as seen in Lyman break galaxies (Adelberger et al. 2003, 2005), (b) redshift clustering of absorbing gas (Scannapieco et al. 2006) or (c) mere chance coincidence of randomly distributed absorbers (Rauch et al. 1997). The core of the Lyα absorption in all three systems where δv(O VI) > 200 km s^{-1} is highly saturated whereas the high velocity components show weak Lyα absorption and relatively strong metal absorption. This could mean that the gas in these high velocity components is highly ionized and possibly of high metallicity. On the other hand, if the three systems where δv(C IV) > 200 km s^{-1} follow the correlation seen in Fig. 11, we expect them to have δv(O VI) > 200 km s^{-1}. However, δv(O VI) could not be measured due to either low S/N (in two cases) or blending with strong Lyα lines. The system at $z_{\rm abs}$= 2.2750 towards HE 2347−4342 is showing unsaturated well connected wide spread Lyα absorption with signature of high ionization. For the other two systems strong C IV is seen with heavily saturated Lyα. The system at $z_{\rm abs}$= 2.8265 towards HE 0940−1050 which shows largest velocity spread (δv(C IV) ~ 375 km s^{-1}) for C IV in our sample is possibly associated with a Lyman break galaxy (LBG) at an impact parameter of 150 h^{-1} kpc (Crighton et al. 2011). Hence it is extremely important to have a detailed spectroscopic survey of galaxies around the redshifts of such large δv systems to understand the possible origin of O VI absorbers.

5.2 Correlation of δv with other parameters

In this section we explore any possible correlation between δv and other observable parameters (see Fig. 13). The strongest correlation is seen between δv(O VI) and N(O VI). The Spearman rank correlation coefficient is 0.72 and the correlation is confirmed at 5.3σ level. While systems with low δv are seen over a wide range of N(O VI), the systems with $\delta v \geq 100$ km s^{-1} are seen when log N(O VI) $\gtrsim 14$. Thus the above mentioned correlation is due to the lower envelop one can see in the figure. As δv is mainly related to the number of components, this lower envelop can not be attributed to a detection bias. This is confirmed by the presence of a significant correlation (i.e. ρ_s = 0.64 with a 4.0σ significance) even when we restrict our analysis to systems with log N(O VI) > 13.7.

Interestingly, a similar correlation is also seen between N(C IV) and δv(C IV) (i.e. ρ_s = 0.57 with a 5.8σ significance). The correlation is significant even when we restrict our analysis to systems with log N(C IV) > 12.6 (i.e. ρ_s = 0.42 with a 3.7σ significance). These results are consistent with what is seen in Fig. 9 of Songaila (2006), who found C IV systems with peak optical depth greater than 0.4 to show larger velocity extent compared to systems with lower peak optical depth. Songaila (2006) suggested that some of the wider C IV systems found among those with high peak optical depth could be associated with galaxy outflows.

We also find a 3σ correlation between δv(O VI) and N(H I) and a 4.5σ correlation between δv(C IV) and N(H I). It is clear from Fig. 13 that for both O VI and C IV, $\delta v \geq 100$ km s^{-1} is seen mainly in systems with log N(H I) $\gtrsim 15$. Such high column densities are generally associated with high over density regions (see e.g., Schaye 2001). In the following section, we show that the systems with log N(H I) > 15.0 have associated low ion absorption. Low ions usually trace higher density regions if the gas is photoionized by the meta-galactic UV radiation (see e.g., Rauch et al. 1997). All these suggest that the O VI or C IV absorbing gas with high velocity spread is probably related to overdense regions. We do not find any strong correlation between δv(O VI) or δv(C IV) with either redshift, N(O VI)/N(C IV) or N(O VI)/N(H I).

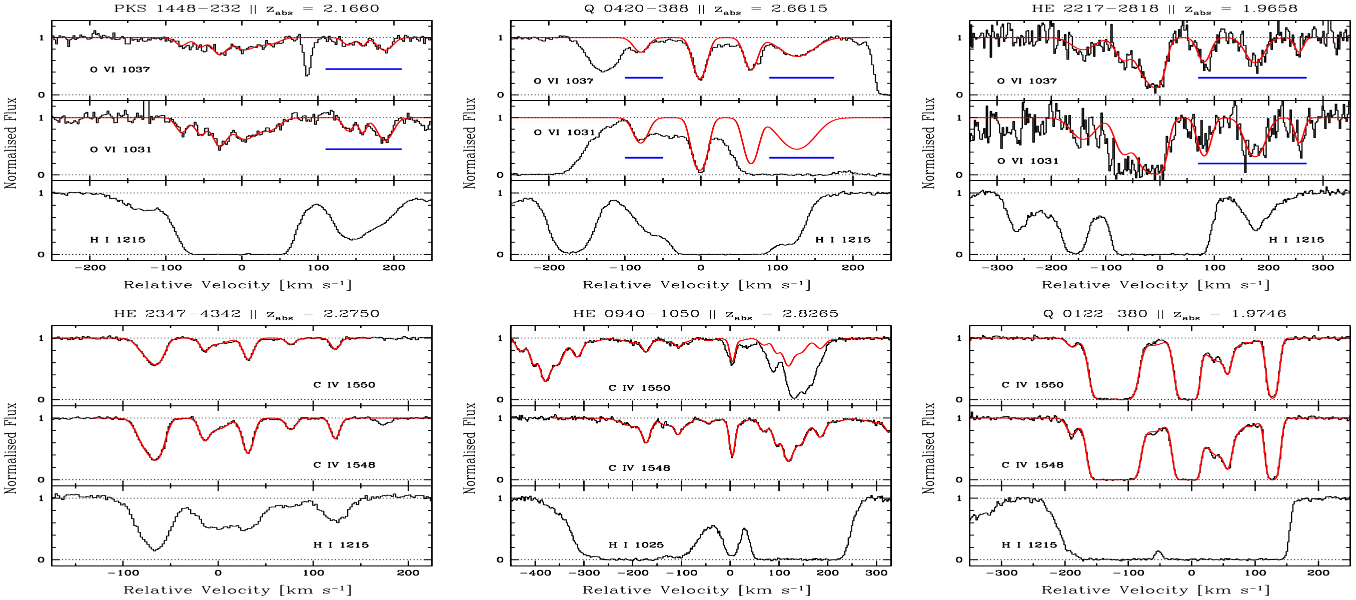

Figure 12. Absorption profiles of systems with $\delta v(\text{O VI}) > 200$ km s^{-1} (top panel) and $\delta v(\text{C IV}) > 200$ km s^{-1} (bottom panel) together with best fitted Voigt profile. The high velocity components identified with solid horizontal bars are showing high ionization. The absorption redshift that defines the zero velocity and the name of the background QSO are also indicated.

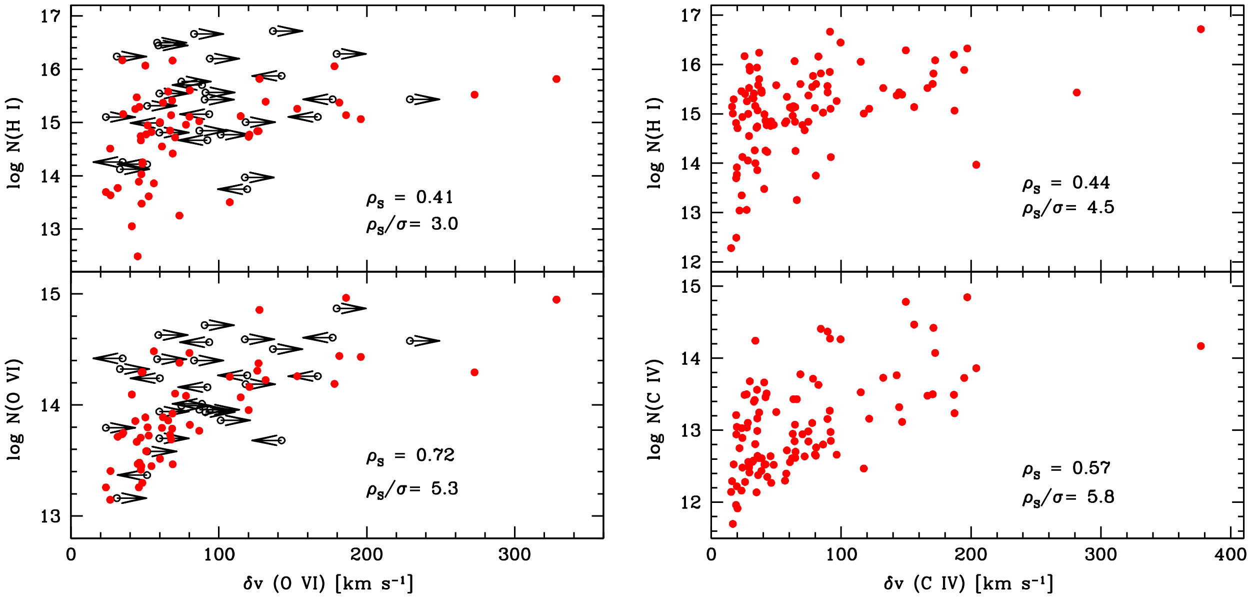

Figure 13. Relationship between δv and other measurable quantities. The results of Spearman test performed for the systems using only the detections of δv (filled circles) are mentioned in each panel.

5.3 Velocity shift (Δv) distribution

In this section, we discuss the velocity offset between the O VI and C IV absorption originating from the same system. Here, we do not attempt to estimate the offset between individual components as our main aim is to find the optical depth weighted phase separation between C IV and O VI and how this is related to other measurable quantities. In most of the cases, the O VI absorption is wider than the C IV one (see section 5.1) and has a larger number of components. We use only systems where both C IV and O VI profiles are well defined at least in one of the doublets and calculate the optical depth weighted redshifts (i.e. $\bar{z}_{\text{O VI}}$ and $\bar{z}_{\text{C IV}}$). The velocity shift between these two redshifts is then,

$$|\Delta v(\text{O VI} - \text{C IV})| = [|(\bar{z}_{\text{O VI}} - \bar{z}_{\text{C IV}})|/(1+\bar{z}_{\text{C IV}})] \times c, \qquad (6)$$

where c is the speed of light in km s^{-1}. The values of $|\Delta v(\text{O VI}-\text{C IV})|$ measurements are summarized in Table 1. In the left most panel of Fig. 14, we plot the distribution of $|\Delta v(\text{O VI} - \text{C IV})|$. The values of the velocity shift are found to be in the range $0 \leq |\Delta v(\text{O VI}-\text{C IV})| \leq 48$ km s^{-1} with a median value of 8 km s^{-1}. We find that only $\sim 9\%$

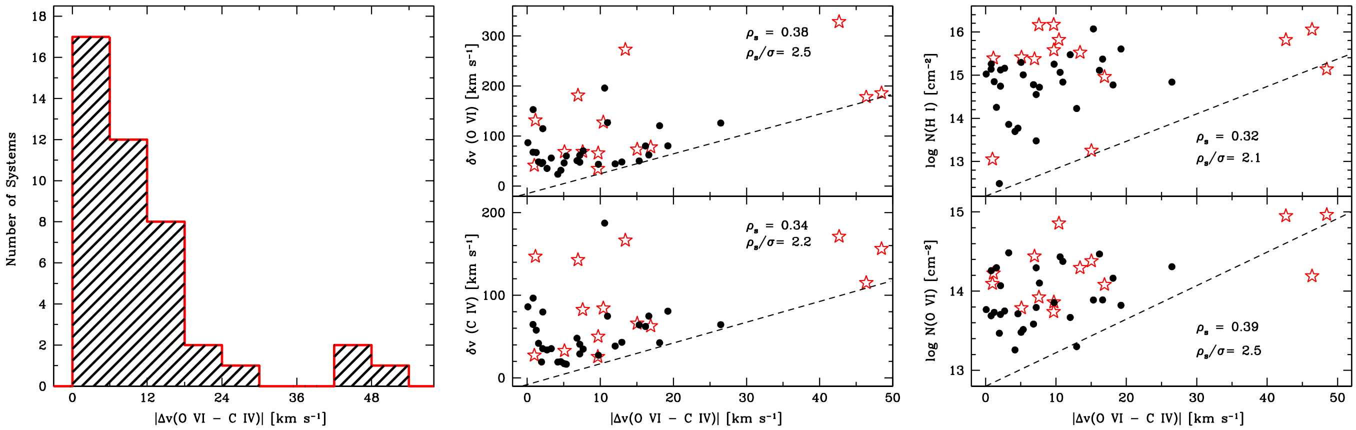

Figure 14. *Left* : The distribution of the velocity shift between the optical depth weighted redshifts of C iv and O vi. *Middle* : The velocity shift, $|\Delta v(\text{O vi} - \text{C iv})|$ versus δv(C iv) (bottom) and δv(O vi) (top). *Right* : The velocity shift, $|\Delta v(\text{O vi} - \text{C iv})|$ versus N(O vi) (bottom) and N(H i) (top). The dashed lines in the middle and right panels are for illustrative purpose to emphasize the possible presence of a lower envelop. The (red) stars in both the panels represent systems with low ions. The results of Spearman rank correlation analysis for all the data points are also summarized in each panel.

of the systems show $|\Delta v(\text{O vi} - \text{C iv})| > 20$ km s^{-1} whereas ~ 33% of the systems have $|\Delta v(\text{O vi} - \text{C iv})| \leq 5$ km s^{-1}. It is to be remembered that the systems with large variation in N(O vi)/N(C iv) ratio from one component to another tend to have large values of $|\Delta v(\text{O vi} - \text{C iv})|$. Hence $|\Delta v(\text{O vi} - \text{C iv})|$ can be seen as a measure of the ionization inhomogeneity among components. Our analysis suggests that O vi systems with large ionization inhomogeneities across the profile are rare. In addition, the median value of the velocity shift distribution for systems with low ions (~ 10.4 km s^{-1}) is higher than that for systems without low ions (~ 6.8 km s^{-1}). Hence, the ionization inhomogeneity seems to be more important in the systems where low ions are detected. But due to the small number of data points the KS test do not show any significant difference between the shift distributions for systems with and without low ions.

We find a mild (at ~ 2.5σ significance level) correlation between either δv(O vi) or N(O vi) and $|\Delta v(\text{O vi} - \text{C iv})|$ (see Fig. 14). These correlations are dominated by the fact that systems with $|\Delta v(\text{O vi} - \text{C iv})| \geq 20$ km s^{-1} are predominantly coming from systems with δv(O vi) $\geq$ 100 km s^{-1} and log N(O vi)(cm^{-2}) $\geq$ 14. A similar trend is also seen for δv(C iv) and N(H i) possibly due to the presence of a lower envelop. However, we find none of the other parameters (i.e., z, N(O vi)/N(H i), N(C iv)/N(H i) and N(O vi)/N(C iv)) showing any significant correlation with $|\Delta v(\text{O vi} - \text{C iv})|$.

6 ANALYSIS BASED ON TOTAL COLUMN DENSITIES

Here we study the distributions of measured column densities of different species, their ratios and dependencies between them. Upper limits are not considered for the analysis.

6.1 Redshift evolution of column density ratios

In Fig. 15 we plot the redshift evolution of various column density ratios. In all the panels (red) stars represent systems with detectable low ions and (black) open circles are for systems without low ions.

The Spearman rank correlation analysis performed between various column density ratios and redshift do not reveal any significant correlation. We also find that the presence of low ions does not influence this result. One of the interesting features of the left most panel in Fig. 15 is the scarcity of data points with log N(O vi)/N(H i) > -0.5 for $z > 2.5$. Bergeron & Herbert-Fort (2005) identified such systems as a separate population of O vi absorbers with high metallicity (see also Schaye et al. 2007). Such high values of N(O vi)/N(H i) ratio are also seen in proximate O vi absorbers (Fox et al. 2008; Tripp et al. 2008). Therefore, these absorbers may either trace high metallicity gas or regions ionized by AGN like sources. Hence, confirming the redshift evolution of these absorbers will be very important. It is to be noted that similar trend (i.e., lack of data points with high N(C iv) to N(H i) ratio for $z > 2.5$) is apparent from the right most panel of Fig. 15. The median values of various column density ratios are also shown in Fig. 15 with horizontal lines. The difference of median values for systems with and without low ions is maximum for N(C iv)/N(O vi) ratio (factor ~ 4). A two sided KS test shows that their distributions are different with very high significance (D = 0.55 & Prob. = 2.6×10^{-5}).

6.2 Relationship between column densities of various species and viability of photoionization model

In this section, we investigate the total column densities of various species and any correlation between them. We compare these with simple photoionization model predictions using "CLOUDY v(07.02)" (Ferland et al. 1998). We would like to point out here that such a single phase photoionization model may oversimplify the problem in view of the possible multiphase structure of the absorbing gas, but such models are often used as a guideline to draw broad conclusions on the nature of the O vi absorbers (e.g. see, Simcoe et al. 2002; Carswell et al. 2002; Bergeron et al. 2002; Bergeron & Herbert-Fort 2005; Schaye et al. 2007; Muzahid et al. 2011).

The model assumes the absorbing gas to be an optically thin plane parallel slab illuminated by the meta-galactic UV background radiation contributed by QSOs and Lyman break galaxies at the median redshift (i.e. z = 2.3) of our survey. We use "HM05" background radiation available in CLOUDY v(07.02) based on the UV spectrum calculated using the method described in

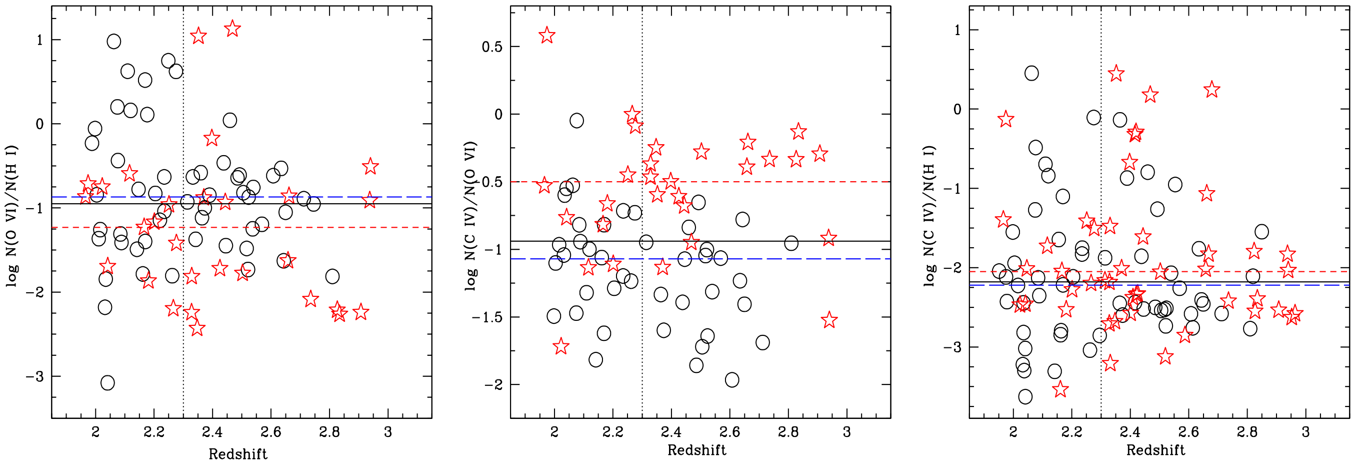

Figure 15. Redshift evolution of O VI to H I (*Left*) C IV to O VI (*Middle*) and C IV to H I (*Right*) column density ratio. In all the panels the (red) stars are the systems with low ions and (black) open circles are the systems without any low ions. The vertical dotted line shows the median redshift of our sample. The median values of column density ratio for the full sample (solid horizontal line), systems with low ions (short dashed line) and systems without low ions (long dashed line) are also indicated in each panel.

Haardt & Madau (1996). For simplicity, we assumed solar relative abundances and run our model with two different values of metallicities (i.e. $Z = 0.1$ and $0.01\ Z_\odot$). In this model, we incorporate the relation between the particle density and the observed H I column density as given in Schaye (2001), i.e.,

$$N(\mathrm{H\,I}) \sim 2.7\times10^{13}\mathrm{cm}^{-2}(1+\delta)^{3/2}T_4^{-0.26}\,\Gamma_{12}^{-1} \times\left(\frac{1+z}{4}\right)^{9/2}\left(\frac{\Omega_\mathrm{b}h^2}{0.02}\right)^{3/2}\left(\frac{f_\mathrm{g}}{0.16}\right)^{1/2}\times\kappa, \tag{7}$$

where, δ denotes over-density, f_g is the gas mass fraction normalised to it's universal value (i.e. Ω_b/Ω_m). All other symbols have their usual meaning. We have introduced a fudge factor called κ and run this model for three different values of κ (0.5, 1 and 2). For the original equation of Schaye (2001), $\kappa = 1$. Hence, for a given $N(\mathrm{H\,I})$, $\kappa > 1$ implies lower density (higher ionization parameter) compared to what is predicted by Schaye (2001). The temperature is calculated from the standard $T - \delta$ relation given by Hui & Gnedin (1997) i.e. $T = T_0\ \delta^{\gamma-1}$ with $T_0 = 2\times10^4$ K and $\gamma = 1.1$. This temperature is very close to the photoionization temperature for the density range of interest here.

6.2.1 *N*(*O* VI) *vs N*(*H* I)

In the panel-(A) of Fig. 16 we plot $N(\mathrm{O\,VI})$ against $N(\mathrm{H\,I})$ for individual O VI systems. Note that $N(\mathrm{O\,VI})$ is varying only ~ 2 dex over a ~ 5 dex variation in $N(\mathrm{H\,I})$. The Spearman rank correlation analysis shows only a mild correlation (at $\sim 2.5\sigma$ level) between $N(\mathrm{H\,I})$ and $N(\mathrm{O\,VI})$ when we consider the full sample. The subsamples of systems with and without low ions do not show any trend between $N(\mathrm{H\,I})$ and $N(\mathrm{O\,VI})$ individually.

It is apparent from the figure, that apart from two systems, low ions are detected in systems with higher H I column density (i.e. $\log N(\mathrm{H\,I}) > 14.6$). The median values of $\log N(\mathrm{H\,I})$ are 15.58 and 14.82 for systems with and without low ions respectively. The KS test shows that the distributions of $N(\mathrm{H\,I})$ in systems with and without low ions are different with very high significance (D = 0.52 and Prob. = 2.1×10^{-7}). It is interesting to note that 36 out of 46 systems where we detect low ions show $\log N(\mathrm{H\,I}) > 15.0$. This could mean that $N(\mathrm{H\,I})$ is predominantly coming from the low ionization phase of the absorbing gas whenever low ions are detected. This is why we do not use systems with low ions (even when metals are aligned with H I) when we measure thermal and non-thermal contribution to the *b*-parameter in section 4.2. Although there is no statistically significant trend between $N(\mathrm{O\,VI})$ and $N(\mathrm{H\,I})$, the O VI column density seems to be systematically higher when low ions are present. The median value of $\log N(\mathrm{O\,VI})$ for systems with low ions is found to be 0.4 dex higher compared to that of the systems without low ions. A two sided KS test shows that the $N(\mathrm{O\,VI})$ distribution between systems with and without low ions are indeed different (D = 0.44 and Prob. = 7.3×10^{-4}).

It is evident from the model curves that the systems with $\log N(\mathrm{H\,I}) > 14.5$ can be roughly reproduced by our simple model for metallicity ranging from 0.01 to 0.1 $Z_\odot$. The systems in the top-right corner of the figure can also be reproduced with higher κ values (i.e. $\kappa \gtrsim 5$) and with low metallicity (i.e. $\sim 0.01Z_\odot$). It is to be remembered that associating entire H I column density measured in a system to the O VI bearing phase will essentially underestimate the metallicity. If, in case of systems with low ions, most of the H I comes from the lower ionization phase then the (red) stars will move towards the left in this plot requiring higher metallicities. Most interestingly, the systems with $\log N(\mathrm{H\,I}) < 14.5$ and $\log N(\mathrm{O\,VI}) > 14.0$ can not be reproduced by our simple model with metallicity $Z = 0.01Z_\odot$ (thin curves) irrespective of the κ values used. These systems require metallicity $\gtrsim 0.1Z_\odot$ provided the ionization is dominated by the meta-galactic UV background.

In the low redshift studies, the $N(\mathrm{H\,I})/N(\mathrm{O\,VI})$ vs $N(\mathrm{H\,I})$ plot is used as an indicator of multiphase medium. For collisional ionization, the O VI ionization fraction peaks at $\sim 10^{5.5\pm0.3}$ K (see Sutherland & Dopita 1993; Gnat & Sternberg 2007) and hence O VI is the most promising species in the UV-optical regime to probe the hard-to-detect hot gas phase in the intergalactic medium, namely, the WHIM. On the other hand most of the Lyα lines are believed to trace relatively cool ($T\sim$ few $\times10^4$ K) photoionized gas, namely, the warm ionized medium. To investigate the relative importance of the warm photoionized and hot collisionally ionized gas, it is customary to plot the "multiphase ratio" i.e. $N(\mathrm{H\,I})/N(\mathrm{O\,VI})$ against $N(\mathrm{H\,I})$ (see Shull et al. 2003; Danforth & Shull 2005). Panel-(B) of Fig. 16

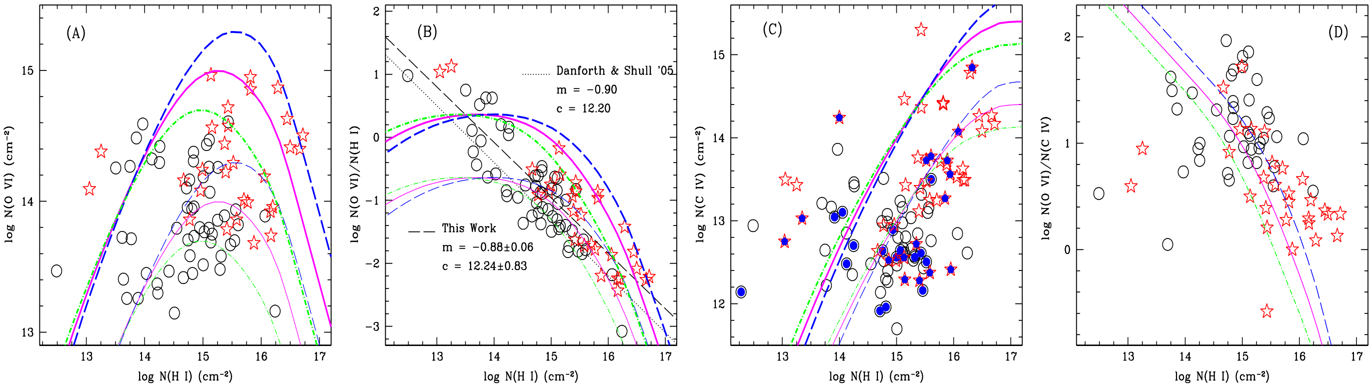

Figure 16. (A) O vi column density against H i column density. In all panels the (red) stars and the (black) circles represent systems with and without low ions respectively. The dot-dashed, solid, and long-dashed curves indicate the results of the photoionization model for $\kappa = 0.5$, 1.0, and 2.0 respectively. The thin and thick curves correspond to metallicities $0.01Z_{\odot}$ and $0.1Z_{\odot}$. **(B)** O vi to H i column density ratios in O vi systems as a function of N(H i). The long-dashed line shows the power law fit to our data. The dotted line shows the fit obtained by Danforth & Shull (2005) for their low-z O vi sample. **(C)** C iv column density against H i column density. The shaded ones are the systems where only upper limits on N(O vi) can be estimated. **(D)** N(O vi)/N(C iv) column density ratio against N(H i). Since the N(O vi) to N(C iv) column density ratio is independent of metallicity we show the curves for only $Z = 0.01Z_{\odot}$.

is a very similar plot and it reveals a strong anti-correlation between N(O vi)/N(H i) and N(H i). This is not very surprising because it is the manifestation of N(O vi) being not strongly correlated with N(H i). Note that the best fit straight line to our data (dashed line) gives a slope and intercept very similar to what is obtained at low redshift (dotted line) by Danforth & Shull (2005). We find that the systems with low ions show slightly higher N(O vi)/N(H i) value for a given N(H i). However, the slope of the best fitted straight lines for systems with and without low ions are very similar.

6.2.2 *N(C iv) vs N(H i)*

Unlike N(O vi), N(C iv) seems to be correlated with N(H i) (see panel-(C) of Fig. 16). A Spearman rank correlation analysis suggests a correlation with rank coefficient $\rho_s = 0.41$ and a 4.2σ significance level. We find that this correlation is mainly dominated by the systems with low ions. In fact no trend is seen between N(C iv) and N(H i) for systems without low ions. The shaded points in this panel represent the systems where we have upper limits on O vi column density as listed in Table 2, and they are predominantly lying in the lower half plane. The median value of log N(C iv) (i.e. 12.64) in these systems is 0.5 dex less than that for the rest of the systems. A two sided KS test indeed shows that the distribution of these points are different from the rest of the data points with ~ 98% probability. The non-detection of O vi in most of these systems is consistent with the average N(O vi)/N(C iv) ratio in our sample.

The trend of increasing N(C iv) with N(H i) is well reproduced by our simple model. Unlike in the case of N(O vi), the difference in the predicted curves at a given N(H i) and metallicity is very small for the range of κ used in our models (in particular for $14 \leq \log N(\text{H i}) \leq 16$). Again here, most of the systems with log N(H i) > 14.5 can be well accommodated with the model curves for metallicity ranging from 0.001 to 0.1 $Z_{\odot}$. On the other hand systems with log N(H i) < 14.5 and log N(C iv) $\gtrsim 13$ require metallicity $Z \gtrsim 0.1Z_{\odot}$ irrespective of κ.

6.2.3 *N(O vi)/N(C iv) vs N(H i)*

In panel-(D) of Fig. 16, the N(O vi)/N(C iv) ratio is plotted against the H i column density. A strong anti-correlation ($\sim$ 4.3σ level) is seen between N(O vi)/N(C iv) and N(H i). Since N(O vi) shows a mild correlation whereas N(C iv) shows strong correlation with N(H i), such anti-correlation is expected. It is to be noted that the anti-correlation seen in the full sample is again dominated by the systems with low ions. No trend is suggested by Spearman rank correlation analysis for the systems without low ions. As the O vi to C iv column density ratio mainly depends on the ionization parameter in this single phase model both the thick and thin curves fall on top of each other. Note that the observed anti-correlation is well reproduced by our model apart from a few systems with very low N(H i).

7 SUMMARY & CONCLUSIONS

We presented a detailed analysis of 84 O vi and 105 C iv systems at $z \sim 2.3$ detected in high resolution ($R \sim 45{,}000$) spectra of 18 bright QSOs observed with VLT/UVES. Here we summarize the main results of our survey.

- **Multiphase nature of the gas :** Consistent with the previous studies, we show that O vi components have systematically wider Doppler parameters (b) compared to those of C iv components. We also show that the line spread (δv) of C iv and O vi are strongly correlated. Therefore we conclude that the metal absorbing regions in the IGM consist of multiphase gas correlated over large velocities.

We do not find any trend between N(O vi) and N(H i), over five orders of magnitude spread in N(H i) but there is a 3σ level correlation between line spread of O vi and N(H i) which possibly suggests that the H i and O vi occur in different phases of a correlated structure. Indeed, Fox (2011) recently argued that the constancy of N(O vi) over a range of N(H i) can be reconciled if O vi absorption originate from conductive, turbulent or shocked boundary layers between warm and hot plasma. Such models are considered to explain the multiphase structure seen in different components of our galaxy (Savage & Sembach 1994; Savage et al. 2003; Spitzer 1996; Sembach et al. 2003; Collins et al. 2004, 2005; Lehner et al. 2011). Existing simulations of metals in the IGM roughly predict such a multiphase correlated structure where O vi absorption originates from low density and extended region whereas C iv originates from regions of slightly higher density (e.g., Rauch et al. 1997; Kawata & Rauch 2007; Fangano et al. 2007; Oppenheimer & Davé 2009; Cen & Chisari 2011).

- **Thermal state of the gas and non-thermal velocities :** The observations presented here are inconsistent with most of the gas associated with the O VI absorption (at $z \sim 2.3$) being in collisional ionization equilibrium (i.e. with $T \sim (2-3)\times10^5$ K). We draw this conclusion mainly from the b(O VI) distribution. Using a subsample of well aligned O VI components we find the median gas temperature is $\sim 3\times10^4$ K with none of the components having $T > 2\times10^5$ K. However, 42% of these well aligned components show $4.6 \le \log T \le 5.0$, which is warmer than the temperature expected in pure photoionization equilibrium. In case of rapidly cooling over-ionized gas such temperatures are expected provided the gas abundance is close to the solar value (see Gnat & Sternberg 2007). The estimated non-thermal contribution to the b-parameter using the b(O VI)–b(H I) pairs are in the range $3.6 \le b_{nt}(\mathrm{km\ s^{-1}}) \le 21.2$ with a median value of 8.2 km s^{-1}. This is consistent with the previous measurements of intergalactic turbulence by Rauch et al. (1996, 2001).

- **Column density distribution :** The O VI column density distribution is well fitted by a power-law with indices $\beta = 1.9 \pm 0.1$ and 2.4 ± 0.2 for systems and components respectively for $\log N$(O VI) > 13.7. We find the distribution is flatter in the case of C IV with respective β values of 1.6 ± 0.1 and 1.9 ± 0.1 down to $\log N$(C IV) $= 12.6$. For both C IV and O VI the β values measured for the components are higher compared to that measured for systems. This is a natural consequence of the fact that the systems with higher column density having systematically higher number of components. While we could not make precise comparisons of these results with the predictions of existing simulations, it is interesting to note that some of the simulations (with or without feedback) produce similar trends (see for example Fig. 10 of Rauch et al. 1997). Cen & Chisari (2011) have found a steeper slope for the N(O VI) distribution compared to that of C IV. They attributed this to the existence of transient structures stemming from the shock heated regions in the neighborhood of galaxies.

- **Gas kinematics :** A strong correlation (5.3σ level) is seen between the velocity spreads (δv) of O VI and C IV. However, δv(C IV) is systematically lower than δv(O VI). We find that both δv(O VI) and δv(C IV) are strongly correlated ($> 5\sigma$ level) with their respective column densities and slightly less (3 and 4.5σ respectively) correlated with N(H I). We note that O VI and/or C IV systems with large velocity spread also show associated low ion absorption lines. As the low ions (as well as strong H I absorption) are expected to originate from high density regions, we conclude that systems with large velocity spread are probably associated with regions of high density. We measured the velocity offset, $|\Delta v$(O VI – C IV)$|$, between optical depth weighted redshifts of C IV and O VI absorption, which is found to be in the range $0 \le |\Delta v$(O VI – C IV)$| \le 48$ km s^{-1} with a median value of 8 km s^{-1}. The systems with low ions seem to have higher velocity shift which possibly indicates higher ionization inhomogeneity in these absorbers. We do not find any strong correlation between $|\Delta v$(O VI – C IV)$|$ and other observable parameters.

- **Total column densities and their ratios :** The total column densities of different species (i.e. H I, C IV, and O VI) seem to be affected by the presence of low ions. The median values of N(H I), N(O VI) and N(C IV) are found to be higher when low ions are present. A two sided KS test suggests that the column density distributions for systems with and without low ions are significantly different. Almost $\sim$ 80% of the systems with low ions show $\log N$(H I) > 15.0 indicating that considerable H I absorption may be originating from the low ionization phase. We find a strong correlation ($\sim 4.3\sigma$) between N(C IV) and N(H I) which is dominated by the systems with low ions. We do not find any clear evidence for the column density ratios (i.e. N(O VI)/N(H I), N(C IV)/N(H I) and N(O VI)/N(C IV)) to evolve with redshift over the range $1.9 \le z \le 3.1$. We find only a tentative evidence for number of systems with high $\log N$(O VI)/N(H I) (e.g., ≥ -0.5 dex) to decrease with increasing redshift. A similar trend is also present for N(C IV)/N(H I) ratio.

- **Comparison between low and high-*z* O VI absorbers :** The b-parameter distribution of O VI components of our sample is significantly different from that of the low-z sample of Tripp et al. (2008). The median value of b(O VI) at low-z is twice as high as at high-z (see also Fox 2011). In addition, the median $b_{\rm nt}$ value for the well aligned components in our sample is a factor ~ 2 less than what is found by Tripp et al. (2008). Interestingly the median value of the temperature measured in these well aligned components is found to be the same (i.e. $T \sim 3\times10^4$K) in both high and low-z sample. All these are consistent with the non-thermal contribution to b(O VI) being higher at low-z. In the models of Evoli & Ferrara (2011) where the turbulence induced by supernova driven winds is considered, the volume-weighted b-parameter remains roughly constant between $z = 2$ to $z = 0$ [see their Fig. 6]. Such a case is not supported by our observations. We speculate that the excess of turbulence at low-z may originate from shocks due to structure formation.

At low redshift, a few thermally broadened Lyα absorbers (BLAs) are seen with signature of high temperature ($T \sim 10^6$ K) gas (Sembach et al. 2004; Richter et al. 2004, 2006; Danforth et al. 2010; Savage et al. 2011). We do not detect such systems in our high-z sample. This may be related to difficulties in detecting broad and shallow absorption features in the dense Lyα forest.

At $z \sim 2.3$ we find the cosmic density of O VI absorbers, $\Omega_{\rm O\,VI} = (1.0\pm0.2)\times10^{-7}$ for $\log N$(O VI) > 13.7. This should be treated as a lower limit as (a) we have not applied the correction factor to redshift path length due to Lyα line blanketing in the forest, (b) the CDDF of O VI is steep and $\Omega_{\rm O\,VI}$ may increase when contributions of numerous low column density systems are included. We calculate the lower limits on the baryonic content of the O VI absorbers assuming (i) ionization fraction of O VI, $f_{\rm O\,VI} = 0.2$, (ii) the average metallicity of the O VI bearing gas is 10% of the solar value as assumed in the low-z studies of O VI absorbers (see, Tripp et al. 2000; Savage et al. 2002; Sembach et al. 2004; Danforth & Shull 2005; Lehner et al. 2006; Danforth & Shull 2008). Most of these papers have shown that low redshift O VI absorbers harbor roughly 5–10% of the baryons in the nearby universe. We find this contribution to be 2.8% at $z \sim 2.3$. The correction to the redshift path length due to line blanketing (as suggested by Simcoe et al. 2002) will increase it up to $\sim$ 7%. Therefore within allowed uncertainties, $\Omega^{\rm O\,VI}_{\rm IGM}$ at $z \sim 0$ is consistent with what we found at $z \sim 2.3$. If O VI predominantly traces a hot phase of the IGM (i.e. $T > 10^5$ K) at every epoch then most numerical simulations (Cen & Ostriker 1999; Davé et al. 2001; Fang & Bryan 2001; Chen et al. 2003; Cen & Chisari 2011) suggest a strong increase in $\Omega^{\rm O\,VI}_{\rm IGM}$ with decreasing redshift. These simulations also suggest that the fraction of baryons at $T < 10^5$ K decreases with decreasing z. Therefore the near constancy of $\Omega^{\rm O\,VI}_{\rm IGM}$ with redshift probably means that the O VI absorbers at high and low redshift may not originate from regions with similar physical conditions.

8 ACKNOWLEDGMENT

We thank the anonymous referee for useful comments that significantly improve this paper. SM thanks CSIR for providing support for this work. RS and PPJ acknowledge support from the Indo-French Centre for the Promotion of Advanced Research under the programme No.4304–2. We thank Pushpa Khare, Anand Narayanan, Kandaswamy Subramanian for useful discussions.

REFERENCES

Adelberger, K. L., Shapley, A. E., Steidel, C. C., Pettini, M., Erb, D. K., & Reddy, N. A., 2005, ApJ, 629, 636

Adelberger, K. L., Steidel, C. C., Shapley, A. E., & Pettini, M., 2003, ApJ, 584, 45

Agafonova, I. I., Levshakov, S. A., Reimers, D., Fechner, C., Tytler, D., Simcoe, R. A., & Songaila, A., 2007, A&A, 461, 893

Aguirre, A., Dow-Hygelund, C., Schaye, J., & Theuns, T., 2008, ApJ, 689, 851

Aguirre, A., Schaye, J., Hernquist, L., Kay, S., Springel, V., & Theuns, T., 2005, ApJ, 620, L13

Aracil, B., Petitjean, P., Pichon, C., & Bergeron, J., 2004, A&A, 419, 811

Ballester, P., Modigliani, A., Boitquin, O., Cristiani, S., Hanuschik, R., Kauffer, A., & Wolf, S., 2000, The Messenger, 101, 31

Becker, G. D., Rauch, M., & Sargent, W. L. W., 2009, ApJ, 698, 1010

Becker, G. D., Sargent, W. L. W., Rauch, M., & Simcoe, R. A., 2006, ApJ, 640, 69

Bergeron, J., Aracil, B., Petitjean, P., & Pichon, C., 2002, A&A, 396, L11

Bergeron, J. & Herbert-Fort, S., 2005, ArXiv Astrophysics e-prints (astro-ph/0506700)

Bergeron, J., Petitjean, P., Aracil, B., et al., 2004, The Messenger, 118, 40

Boksenberg, A., Sargent, W. L. W., & Rauch, M., 2003, ArXiv Astrophysics e-prints (astro-ph/0307557)

Buote, D. A., Zappacosta, L., Fang, T., Humphrey, P. J., Gastaldello, F., & Tagliaferri, G., 2009, ApJ, 695, 1351

Carswell, B., Schaye, J., & Kim, T., 2002, ApJ, 578, 43

Cen, R. & Chisari, N. E., 2011, ApJ, 731, 11

Cen, R. & Ostriker, J. P., 1999, ApJ, 514, 1

—, 2006, ApJ, 650, 560

Chand, H., Srianand, R., Petitjean, P., & Aracil, B., 2004, A&A, 417, 853

Chen, X., Weinberg, D. H., Katz, N., & Davé, R., 2003, ApJ, 594, 42

Collins, J. A., Shull, J. M., & Giroux, M. L., 2004, ApJ, 605, 216

—, 2005, ApJ, 623, 196

Cooksey, K. L., Thom, C., Prochaska, J. X., & Chen, H.-W., 2010, ApJ, 708, 868

Cowie, L. L., Hu, E. M., & Songaila, A., 1995a, Nature, 377, 603

—, 1995b, AJ, 110, 1576

Crighton, N. H. M., Bielby, R., Shanks, T., et al., 2011, MNRAS, 414, 28

Danforth, C. W. & Shull, J. M., 2005, ApJ, 624, 555

—, 2008, ApJ, 679, 194

Danforth, C. W., Shull, J. M., Rosenberg, J. L., & Stocke, J. T., 2006, ApJ, 640, 716

Danforth, C. W., Stocke, J. T., & Shull, J. M., 2010, ApJ, 710, 613

Davé, R., Cen, R., Ostriker, J. P., et al., 2001, ApJ, 552, 473

Davé, R., Hernquist, L., Katz, N., & Weinberg, D. H., 1999, ApJ, 511, 521

Dekker, H., D'Odorico, S., Kaufer, A., Delabre, B., & Kotzlowski, H., 2000, in Proc. SPIE, 4008, 534-545

D'Odorico, V., Calura, F., Cristiani, S., & Viel, M., 2010, MNRAS, 401, 2715

Edgar, R. J. & Chevalier, R. A., 1986, ApJ, 310, L27

Edlén, B., 1966, Metrologia, 2, 71

Ellison, S. L., Songaila, A., Schaye, J., & Pettini, M., 2000, AJ, 120, 1175

Evoli, C. & Ferrara, A., 2011, MNRAS, 413, 2721

Fang, T. & Bryan, G. L., 2001, ApJ, 561, L31

Fang, T., Buote, D. A., Humphrey, P. J., Canizares, C. R., Zappacosta, L., Maiolino, R., Tagliaferri, G., & Gastaldello, F., 2010, ApJ, 714, 1715

Fangano, A. P. M., Ferrara, A., & Richter, P., 2007, MNRAS, 381, 469

Ferland, G. J., Korista, K. T., Verner, D. A., Ferguson, J. W., Kingdon, J. B., & Verner, E. M., 1998, PASP, 110, 761

Fox, A. J., 2011, ApJ, 730, 58

Fox, A. J., Bergeron, J., & Petitjean, P., 2008, MNRAS, 388, 1557

Fox, A. J., Petitjean, P., Ledoux, C., & Srianand, R., 2007, A&A, 465, 171

Frank, S., Mathur, S., Pieri, M., & York, D. G., 2010a, AJ, 140, 817

—, 2010b, AJ, 140, 835

Gnat, O. & Sternberg, A., 2007, ApJS, 168, 213

Haardt, F. & Madau, P., 1996, ApJ, 461, 20

Heckman, T. M., Norman, C. A., Strickland, D. K., & Sembach, K. R., 2002, ApJ, 577, 691

Hellsten, U., Hernquist, L., Katz, N., & Weinberg, D. H., 1998, ApJ, 499, 172

Hui, L. & Gnedin, N. Y., 1997, MNRAS, 292, 27

Kang, H., Ryu, D., Cen, R., & Song, D., 2005, ApJ, 620, 21

Kawata, D. & Rauch, M., 2007, ApJ, 663, 38

Ledoux, C., Petitjean, P., Fynbo, J. P. U., Møller, P., & Srianand, R., 2006, A&A, 457, 71

Lehner, N., Prochaska, J. X., Kobulnicky, H. A., Cooksey, K. L., Howk, J. C., Williger, G. M., & Cales, S. L., 2009, ApJ, 694, 734

Lehner, N., Savage, B. D., Wakker, B. P., Sembach, K. R., & Tripp, T. M., 2006, ApJS, 164, 1

Lehner, N., Zech, W. F., Howk, J. C., & Savage, B. D., 2011, ApJ, 727, 46

Muzahid, S., Srianand, R., & Petitjean, P., 2011, MNRAS, 410, 2193

Narayanan, A., Savage, B. D., Wakker, B. P., et al., 2011, ApJ, 730, 15

Narayanan, A., Wakker, B. P., & Savage, B. D., 2009, ApJ, 703, 74

Nicastro, F., Mathur, S., Elvis, M., et al., 2005a, Nature, 433, 495

—, 2005b, ApJ, 629, 700

Oppenheimer, B. D. & Davé, R., 2009, MNRAS, 395, 1875

Petitjean, P. & Bergeron, J., 1994, A&A, 283, 759

Pettini, M., Madau, P., Bolte, M., Prochaska, J. X., Ellison, S. L., & Fan, X., 2003, ApJ, 594, 695

Pieri, M. M., Schaye, J., & Aguirre, A., 2006, ApJ, 638, 45

Rauch, M., Carswell, R. F., Chaffee, F. H., Foltz, C. B., Webb,

J. K., Weymann, R. J., Bechtold, J., & Green, R. F., 1992, ApJ, 390, 387
Rauch, M., Haehnelt, M. G., & Steinmetz, M., 1997, ApJ, 481, 601
Rauch, M., Sargent, W. L. W., & Barlow, T. A., 2001, ApJ, 554, 823
Rauch, M., Sargent, W. L. W., Womble, D. S., & Barlow, T. A., 1996, ApJ, 467, L5
Richter, P., Fang, T., & Bryan, G. L., 2006, A&A, 451, 767
Richter, P., Savage, B. D., Tripp, T. M., & Sembach, K. R., 2004, ApJS, 153, 165
Rollinde, E., Srianand, R., Theuns, T., Petitjean, P., & Chand, H., 2005, MNRAS, 361, 1015
Ryan-Weber, E. V., Pettini, M., & Madau, P., 2006, MNRAS, 371, L78
Ryan-Weber, E. V., Pettini, M., Madau, P., & Zych, B. J., 2009, MNRAS, 395, 1476
Savage, B. D., Lehner, N., Wakker, B. P., Sembach, K. R., & Tripp, T. M., 2005, ApJ, 626, 776
Savage, B. D., Narayanan, A., Lehner, N., & Wakker, B. P., 2011, ApJ, 731, 14
Savage, B. D., Narayanan, A., Wakker, B. P., et al., 2010, ApJ, 719, 1526
Savage, B. D. & Sembach, K. R., 1994, ApJ, 434, 145
Savage, B. D., Sembach, K. R., Tripp, T. M., & Richter, P., 2002, ApJ, 564, 631
Savage, B. D., Sembach, K. R., Wakker, B. P., et al., 2003, ApJS, 146, 125
Scannapieco, E., Pichon, C., Aracil, B., Petitjean, P., Thacker, R. J., Pogosyan, D., Bergeron, J., & Couchman, H. M. P., 2006, MNRAS, 365, 615
Schaye, J., 2001, ApJ, 562, L95
Schaye, J., Aguirre, A., Kim, T.-S., Theuns, T., Rauch, M., & Sargent, W. L. W., 2003, ApJ, 596, 768
Schaye, J., Carswell, R. F., & Kim, T., 2007, MNRAS, 379, 1169
Sembach, K. R., Tripp, T. M., Savage, B. D., & Richter, P., 2004, ApJS, 155, 351
Sembach, K. R., Wakker, B. P., Savage, B. D., et al., 2003, ApJS, 146, 165
Shull, J. M., Tumlinson, J., & Giroux, M. L., 2003, ApJ, 594, L107
Simcoe, R. A., 2006, ApJ, 653, 977
Simcoe, R. A., Sargent, W. L. W., & Rauch, M., 2002, ApJ, 578, 737
—, 2004, ApJ, 606, 92
Simcoe, R. A., Sargent, W. L. W., Rauch, M., & Becker, G., 2006, ApJ, 637, 648
Smith, B. D., Hallman, E. J., Shull, J. M., & O'Shea, B. W., 2011, ApJ, 731, 6
Songaila, A., 2001, ApJ, 561, L153
—, 2005, AJ, 130, 1996
—, 2006, AJ, 131, 24
Songaila, A. & Cowie, L. L., 1996, AJ, 112, 335
Spitzer, Jr., L., 1996, ApJ, 458, L29+
Stocke, J. T., Penton, S. V., Danforth, C. W., Shull, J. M., Tumlinson, J., & McLin, K. M., 2006, ApJ, 641, 217
Storrie-Lombardi, L. J., McMahon, R. G., & Irwin, M. J., 1996, MNRAS, 283, L79
Stumpff, P., 1980, A&AS, 41, 1
Sutherland, R. S. & Dopita, M. A., 1993, ApJS, 88, 253
Thom, C. & Chen, H.-W., 2008, ApJS, 179, 37
Tripp, T. M., Savage, B. D., & Jenkins, E. B., 2000, ApJ, 534, L1
Tripp, T. M., Sembach, K. R., Bowen, D. V., Savage, B. D., Jenkins, E. B., Lehner, N., & Richter, P., 2008, ApJS, 177, 39
Tumlinson, J., Werk, J. K., Thom, C., et al., 2011, ApJ, 733, 111
Wakker, B. P. & Savage, B. D., 2009, ApJS, 182, 378
Webb, J. K., 1987, PhD thesis, Univ. Cambridge, 1987.
Zappacosta, L., Nicastro, F., Maiolino, R., Tagliaferri, G., Buote, D. A., Fang, T., Humphrey, P. J., & Gastaldello, F., 2010, ApJ, 717, 74